

**Comparison of CALIPSO-like, LaRC and MODIS Retrievals of Ice Cloud Properties over
SIRTA in France and Florida during CRYSTAL-FACE**

M. Chiriaco⁽¹⁾, H. Chepfer⁽¹⁾, P. Minnis⁽²⁾, M. Haeffelin⁽¹⁾, S. Platnick⁽³⁾, D. Baumgardner⁽⁴⁾, P. Dubuisson⁽⁵⁾, M. McGill⁽³⁾, V. Noël⁽²⁾, J. Pelon⁽⁶⁾, D. Spangenberg⁽⁷⁾, S. Sun-Mack⁽⁸⁾, G. Wind⁽⁹⁾

(1) Laboratoire de Météorologie Dynamique, IPSL, Palaiseau, France

(2) NASA Langley Research Center, Hampton VA, USA

(3) NASA Goddard Space Flight Center, Greenbelt, USA

(4) Université Autonoma de Mexico, Mexico

(5) ELICO, Université du Littoral, France

(6) Service d'Aéronomie, IPSL, Paris, France

(7) AS&M, Inc., Hampton, VA, USA

(8) SAIC, Hampton, VA, USA

(9) SSAI, Lanham, MD, USA

Submitted to the Journal of Applied Meteorology

April 2005

Corresponding author:

Marjolaine Chiriaco

33 (0)1 69 33 31 94

chiriaco@lmd.polytechnique.fr

Laboratoire de Météorologie Dynamique / IPSL

Ecole Polytechnique

91128 Palaiseau cedex, France

Abstract

This study compares cirrus particle effective radius retrieved by a CALIPSO-like method with two similar methods using MODIS, MODIS Airborne Simulator (MAS), and GOES imagery. The CALIPSO-like method uses lidar measurements coupled with the split-window technique that uses the infrared spectral information contained at the 8.65- μm , 11.15- μm and 12.05- μm bands to infer the microphysical properties of cirrus clouds. The two other methods, using passive remote sensing at visible and infrared wavelengths, are the operational MODIS cloud products (referred to by its archival product identifier MOD06 for MODIS Terra) and MODIS retrievals performed by the CERES team at LaRC (Langley Research Center) in support of CERES algorithms; the two algorithms will be referred to as MOD06- and LaRC-method, respectively.

The three techniques are compared at two different latitudes : (i) the mid-latitude ice clouds study uses 18 days of observations at the Palaiseau ground-based site in France (SIRTA: Site Instrumental de Recherche par Télédétection Atmosphérique) including a ground-based 532-nm lidar and the Moderate resolution Imaging Spectrometer (MODIS) overpasses on the Terra Platform, (ii) the tropical ice clouds study uses 14 different flight legs of observations collected in Florida, during the intensive field experiment CRYSTAL-FACE (Cirrus Regional Study of Tropical Anvils and cirrus Layers – Florida Area Cirrus Experiment), including the airborne Cloud Physics Lidar (CPL) and the MAS.

The comparison of the three methods gives consistent results for the particle effective radius and the optical thickness, but discrepancies in cloud detection and altitudes. The study confirms the value of an active remote-sensing method (CALIPSO-like) for the study of sub-visible ice clouds, in both mid-latitudes and tropics. Nevertheless, this method is not reliable in optically very thick tropical ice clouds.

1. Introduction

Ice clouds play a major role in the radiative energy budget of the earth-atmosphere system (Liou 1986). Their impact is governed primarily by their opposing albedo and greenhouse effects that are poorly known for thin ice clouds. Both the macro- and microphysical properties of ice clouds determine these competing effects. The global coverage, altitude, temperature, vertical structure and spatial inhomogeneities of these clouds must be accurately assessed to quantify their impact on weather and climate. Additionally, ice water content and its spatial distribution are critical to the global radiative effect of cirrus clouds. A large uncertainty in evaluating the radiative impact of ice clouds arises from our limited knowledge of the natural variability of their microphysical properties, such as the size, shape and orientation of ice crystals, which determine their optical characteristics. For example, the effective radius of ice crystals composing cirrus clouds is an important microphysical parameter, as it largely affects cloud albedo, which increases with decreasing effective radius for a fixed ice water path. Reducing the uncertainties in both their macro- and microphysical properties is essential for accurately defining the role of ice clouds in climate.

Satellite data are best suited for estimating ice cloud properties because of their global coverage and long-term monitoring potential. Many remote sensing techniques have been devised to take advantage of the spectral radiances measured from various satellites to retrieve ice cloud properties. The remote sensing methods have been complemented on a local scale by various mid-latitude field experiments, such as the First ISCCP Regional Experiment (FIRE; Randall et al., 1996), the European Cloud and Radiation Experiment (Raschke et al., 1998), the International Cirrus Experiment (Raschke et al., 1990), and the SUBsonic aircraft: Contrail and Cloud Effects Special Study (SUCCESS; Toon and Miake-Lye, 1998) as well as a few tropical campaigns such as the Central Equatorial Pacific EXperiment (CEPEX; McFarquhar and Heymsfield, 1996) and the recent Cirrus Regional Study of Tropical Anvils and cirrus Layers – Florida Area Cirrus Experiment (CRYSTAL-FACE; see Jensen et al., 2004) have collected a wealth of in-situ data that show

significant variability of cirrus cloud particle sizes, either from one cloud to another, or within a single cloud (Heymsfield 1975, Heymsfield and Platt 1984, Heymsfield 1993, Krupp 1991). Improved knowledge of realistic effective radii and shapes of ice crystals on the basis of in-situ measurement has led to an improvement in the computation of the scattering properties of ice crystals (Wendling et al., 1979, Takano and Liou 1989, Macke et al., 1996, Yang and Liou 1998). In parallel, various remote sensing retrieval techniques have been developed to infer the ice crystal effective radii from ground-based observations using active sensors (Platt et al., 1989, Intrieri et al., 1993, Intrieri et al., 1995, Mace et al., 1998, Matrosov 1999) and from satellite observations using passive sensors (Minnis et al., 1998, King et al., 2003, Platnick et al., 2003). In addition to improving the theoretical treatment of cloud optical properties, the in situ data are useful for understanding and evaluating the ground-based and, to some extent, the satellite retrievals. The ground-based retrievals can also be used for verifying the satellite passive remote sensing (e.g., Mace et al., 2004). It is also necessary, however, to determine the level of agreement between different remote sensing methods as another aspect of the uncertainties in the retrieved cloud properties.

A new retrieval algorithm recently developed for the upcoming Cloud-Aerosol Lidar and Infrared Pathfinder Satellite Observations (CALIPSO) mission (Winker et al., 2003) combines both passive and active sensors to retrieve ice particle effective radius. This hybrid technique (Chiriaco et al., 2004) will be implemented to create an operationally archived CALIPSO product. It will use collocated data from the three-channel (8.7, 10.5, and 12 μm) CALIPSO Infrared Imager (IIR) and the 532-nm backscatter lidar operating with polarization capability on CALIPSO. Given the expected CALIPSO launch in 2005, it is important to ensure that the technique operates as expected. The intent of this paper is to perform an initial validation of the ice particle effective radius retrieval algorithm developed for this instrument by Chiriaco et al. (2004) and to compare a few other relevant parameters such as optical thickness and cloud height. This new algorithm is applied to datasets of mid-latitude ice clouds observed at the Site Instrumental de Recherche par Télédétection

Atmosphérique (SIRTA, Haeffelin et al. 2005) in France and of tropical ice clouds observed during the 2002 CRYSTAL-FACE field campaign. The results of these retrievals are compared to two other methods that use passive remote-sensing measurements from the MODerate resolution Imaging Spectroradiometer (MODIS) imager: the algorithm developed for the Clouds and Earth's Radiant Energy System (CERES) measurements by Minnis et al (1995, 1998), and the algorithm developed as part of the operational MODIS cloud product (Platnick et al., 2003). The former method will be referred to as the LaRC algorithm, while the latter is referred to as MOD06 which is the product identifier for the MODIS Terra cloud product in the NASA Goddard Earth Sciences Distributed Active Archive Center (DAAC). LaRC retrievals for a CERES footprint are archived at the NASA Langley DAAC. Differences between MOD06 and a similar algorithm applied to the MODIS Airborne Simulator (MAS) data obtained during CRYSTAL-FACE will be discussed in section 4. For CRYSTAL-FACE analysis, LARC retrievals are applied to GOES imagery. In situ data taken during CRYSTAL-FACE are also used to evaluate both the passive and CALIPSO-like algorithms.

2. Three methods to retrieve ice cloud properties

a. CALIPSO-like method

The CALIPSO-like method retrieves ice cloud properties, in particular, the optical thickness and the effective radius of the ice crystals given a set of measurements similar to those that will be taken by CALIPSO: 532-nm lidar backscattering and brightness temperatures at 8.7, 10.5, and 12 μm . The effective radius r_e initially corresponds to the radius of a sphere with a volume equivalent to the ice crystal one, but it is corrected in order to be defined as:

$$r_e = \frac{3}{4} \frac{V}{A} \quad (1)$$

where V is the particle volume and A is its projected area.

The method (Chiriaco et al., 2004) is based on the Brightness Temperature Differences (BTD) between pairs of infrared channels measured from space. The BTDs are compared to their

counterparts computed for various ice crystal models based on effective radius and aspect ratio derived by Yang et al. (2001) with optical thicknesses ranging from 0 to 50. The brightness temperatures are computed using a radiative transfer code including both scattering and absorption (Dubuisson et al., 2005). The cloud base and top altitudes are determined with the 532-nm lidar. Those altitudes are associated with a collocated radiosonde temperature profile to determine the cloud top and base temperatures. Then, for each cloud case studied, the surface and clear-sky atmospheric properties, as well as the observed cloud temperature at the altitude where the lidar backscattered signal is maximal (Chiriaco et al. in revision), are prescribed in the radiative transfer code. This method is a split window technique, improved by the lidar information. This improvement strongly decreases the uncertainty on effective radius retrieval for semi-transparent clouds (Chiriaco et al. 2004).

For a cloudy atmosphere, various microphysical parameters of particles are used to specify the cloud optical properties in the radiative transfer computations: spherical models and hexagonal models with aspect ratios varying between 0.15 and 9.26, for effective radii varying between 0.5 and 200 μm (Chiriaco et al., 2004). The comparison between the computed and measured BTDs is used to select pairs of r_e and particle aspect ratio Q for several microphysical models that best match the observations. Another constraint uses Q derived from the lidar depolarization with the method of Noel et al. (2002). Four Q classes are defined to roughly segregate particles from the most to the least spherical: class I for $Q < 0.05$, class II for $0.05 < Q < 0.7$, class III for $0.7 < Q < 1.1$, class IV for $Q > 1.1$. This constraint reduces the number of solutions, leading to an optimized selection of a microphysical model as defined by effective radius and particle aspect ratio.

b. LaRC method

The LaRC method was developed for application to operational meteorological satellite imagers for the Atmospheric Radiation Measurement program (ARM, Ackerman and Stokes, 2003)

and for the research satellite imagers used by the CERES project. This method detects clouds and retrieves cloud properties using radiances measured by at 0.65, 3.75, 10.8, and 12.05 μm ; effective particle radius information comes from the 3.75 μm band, but its definition is different from the r_e definition in (1). In order to compare effective radii from the same definition, we use this correction formula:

$$r_e = 0.0025 \times r_0^2 + 0.605 \times r_0 \quad (2)$$

where r_0 is the initial radius from LaRC technique.

The LaRC scene classification technique consists primarily of cascading threshold tests (Trepte et al., 2002). To define a pixel as cloudy, at least one of the spectral radiances must differ significantly from the corresponding expected clear-sky radiances. For a pixel classified as cloudy, the main algorithm used to retrieve cloud properties is the Visible Infrared Solar-Infrared Split-window Technique (VISST), which is a 4-channel upgrade of the 3-channel method of Minnis et al. (1995). Given the clear-sky radiances and surface properties, the VISST computes the spectral radiances expected for both liquid-droplet and ice-water clouds for a range of optical thickness $\tau = 0.25$ to 128 for a particular effective cloud temperature T_c using a set of reflectance and emittance parameterizations (Minnis et al., 1998). The liquid particle effective radii $r_{e,\text{liquid}}$ for the model clouds range from 2 to 32 μm and the effective radii $r_{e,\text{ice}}$ for the hexagonal ice column model clouds vary from 3 to 67.5 μm . The thermodynamical phase is determined by a combination of tests that incorporate the final cloud temperature, the initially derived cloud altitude, and the 10.8 - 12.0 μm brightness temperature difference. When the spectral data are available, the 1.6- μm /0.65- μm reflectance ratio is also used in the phase decision. The effective cloud height is estimated from T_c using vertical profiles of temperature from numerical weather analyses. Cloud-top and base heights are then estimated from empirical data (e.g., Chakrapani et al., 2002). The LaRC technique has been applied to a variety of datasets including the Geostationary Operational Environmental Satellite (GOES) series (e.g., Minnis et al., 2004), the National Oceanic and Atmospheric Administration /

Advanced Very High Resolution Radiometers (NOAA/AVHRR, Young et al., 1998), the Visible Infrared Scanner on the Tropical Rainfall Measuring Mission (TRMM) satellite, and the MODIS on the Terra and Aqua satellites (Minnis et al., 2003). As shown in Table 1, the same version of LaRC method is used for both mid-latitude and tropical ice clouds.

c. MODIS operational method: MOD06

The MOD06 uses several channels of the instrument ranging between 0.65 and 13.3 μm (Platnick et al., 2003; King et al., 2003). The cloud mask uses a series of threshold tests to detect the presence of clouds with 4 confidence levels, with up to 20 bands from visible through the infrared (Ackerman et al., 1998). For mid- to high-level clouds, the cloud top pressure is retrieved using a CO_2 slicing technique (Menzel et al., 1983) that uses ratios of differences in radiances between cloudy and clear-sky regions at two nearby wavelengths. For low-level clouds, the infrared window 11- μm band temperature is used to determine a cloud top temperature, assuming the cloud is optically thick, and a cloud top pressure is assigned by comparing the measured brightness temperature to the National Center for Environmental Prediction (NCEP) Global Data Assimilation System (GDAS) temperature profile (Derber et al., 1991). For the thermodynamic phase retrieval, the method uses the 8.52- and 11- μm bands to exploit the spectral emission differences between water droplets and ice crystals (Baum et al., 2000) as well as ratios of the 1.6 and 2.1 μm bands relative to visible and/or near-infrared bands (King et al., 2004). Cloud optical thickness and r_e are estimated based on library calculations of plane-parallel homogeneous clouds overlying a black surface in the absence of atmosphere. Separate libraries exist for liquid water and ice clouds, the latter consisting of 12 size distributions composed of 4 habits (aggregates, bullet rosettes, hollow columns, and plates) with the fraction of each habit in individual size distribution bins being a function of particle effective radius that is defined as follow:

$$r_e = \frac{3 \langle V \rangle}{4 \langle A \rangle} \quad (3)$$

This definition is equivalent to (1) but for crystals with size distribution: $\langle V \rangle$ is the mean particle volume for the ice crystal size distribution and $\langle A \rangle$ is the mean projected area.

Scattering calculations are made using the techniques of Yang and Liou (1996). The effective radii for these 12 distributions vary from about 6-60 μm (King et al., 2004). The optical thickness and effective radius retrievals are derived from MODIS water-absorbing bands (1.6, 2.1, 3.7 μm) in conjunction with one of the non-absorbing bands (0.65, 0.86, 1.2 μm).

Table 1 shows the differences between the products available for the SARTA cases and the CRYSTAL-FACE cases. The MOD06 retrievals over SARTA use MODIS/Terra data and are archived at the NASA Goddard Distributed Active Archive Center (DAAC). The CRYSTAL-FACE cases are processed independently using radiances from the MAS that flew on the NASA ER-2 aircraft. The MAS retrievals are based on the retrieval method of Platnick et al. (2001) and use ice libraries similar to those described above for MOD06, but with two distinctions. First, new scattering calculations for the 12 distributions were made using MAS-specific spectral band-passes. Second, a quadratic polynomial was fitted to all scattering parameters (single scattering, albedo, asymmetry parameter, and extinction efficiency) as a function of the 12 size distributions in order to smooth out non-monotonic behavior with particle effective radius. Then reflectance libraries were calculated at equal intervals in interpolated r_e space (5, 10... 55, 60 μm). The MAS products include a map of apparent multi-layer clouds that provides information on the confidence of the retrievals. Being a spectrometer, the phase algorithm for MAS includes additional tests which are derived from the location of the MAS band corresponding to the peak reflectance in the 1.6 and 2.1 μm spectral regions (Pilewskie and Twomey, 1987). Finally, the MAS cloud top properties retrievals are not derived from a CO_2 slicing technique, but from an algorithm that uses path absorption in the 0.94- μm water vapor band; NCEP profiles are used to convert vapor path to cloud-top pressure and temperature.

3. Mid-latitude ice clouds: SIRTAs cases

a. Observations: instruments and dates

The SIRTAs observatory sits on a 10-km plateau about 160 m above sea level. The plateau is a semi-urban environment divided equally in agricultural fields, wooded areas, and housing and industrial developments. Eighteen mid-latitude cloud cases observed at the SIRTAs ground-based site are investigated using observations collected with the instruments listed below.

1) *MODIS*. Depending on the orbit, MODIS on Terra observes Palaiseau once or twice per day. Although higher resolution data are available for selected channels, the nominal MODIS resolution is 1 km for all 36 channels. Those data are used in each of the three methods and the pixel areas used for the application are described in Table 2. For all retrievals except MOD06 cloud top pressure and temperature, the sample of pixels is a strip large of 3 pixels wide (i.e. 3 km) and 1 hour long centered on the SIRTAs overpass time (using wind information from radiosonde at the cloud altitude from lidar); for this sample, data are corrected from parallax using the cloud altitude from lidar and the wind speed from the radiosonde. For the MOD06 pressure and temperature retrievals, the sample used is a box of 5x5 pixels (i.e. 5x5 km²) over SIRTAs, as this product is only available at this resolution.

2) *Ground-based 532-nm lidar*. The SIRTAs 532-nm lidar is similar to the one that will be on-board the CALIPSO platform. It operates 4 days per week from 0800-2000 hours local time, with a nominal temporal resolution of 10 seconds (an average of 200 shots) and a vertical resolution of 15 m. It is a zenith viewing lidar that measures both the backscattered signal and linear depolarization ratio. The lidar observations are treated as follows: (i) the parallel-polarized signal at 532-nm is normalized to the molecular signal deduced from the radiosonde profiles (described below), (ii) the cloud base and top altitudes are derived from lidar profiles averaged over 1 minute in the parallel channel using a threshold method, (iii) the linear depolarization ratio is the ratio of the perpendicular to the parallel channel and it is

normalized to 2.8% (Young, 1980) in a cloud-free area, i.e. where there are only atmospheric molecules.

3) *MétéoFrance radiosondes*. The ground-based cloud-top and -base temperatures are derived from the coupling of the cloud altitude (derived from the lidar) with the temperature profile obtained by radiosondes launched twice per day (0000 UTC and 1200 UTC) from the Trappes station as part of the Météo-France operational network, located 15 km away from the SIRTa site.

The studied cases were selected using lidar information. Ice clouds were identified using the depolarization ratio based on the behavior of non-spherical particles (i.e., ice crystals) that strongly depolarize the signal. Furthermore, the boundaries of thin ice clouds are determined from the lidar backscattered signal when both cloud bottom and top are evident in the returns. Only those clouds that are relatively constant (± 30 minutes around the satellite overpass) in time and in space are selected in order to facilitate good collocation between the lidar and the satellite measurements. A total of 18 different days of observations have been analyzed. Table 3 summarizes the dates and time periods of observations for the different instruments as well as the cloud altitudes.

b. Comparison of the three methods

A) Illustrative case: 8 October 2002

Figure 1a shows the evolution of the 532-nm lidar depolarization ratio with time and altitude. This image indicates a cloud located between 6.5 and 11 km with a relatively constant altitude, making it a good case study. The depolarization ratios range between 20% and 60% within the cloud, indicating that it is an ice cloud. Figure 1b shows a pseudo-color image of the area based on the 0.6, 1.6, and 11- μm MODIS channels. Pixels from this image were collocated with the lidar measurements corresponding to time when Terra passed over the SIRTa site (center of the red square) at 1105 UTC. The length of the strip of pixels used for the retrieval is calculated as follow:

each pixel is at a distance d from the SARTA pixel; the horizontal wind (U , V) at the cloud altitude is known from the radiosonde; and the time when the pixel overpasses the SARTA is calculated from d and (U , V). The pixel strip selected for the retrieval is 1 km wide and corresponds to ± 30 min centered on the SARTA site. This strip is represented with red lines in Figure 1a. For this case, $U = 5.79 \text{ m.s}^{-1}$ and $V = 2.43 \text{ m.s}^{-1}$ at the altitude of cloud center, so the strip length is approximately 22 km. Figure 1c shows the cloud phase retrieved from the LaRC method. In the red square centered on the SARTA site, most of pixels are ice clouds, with a few pixels of water cloud or clear sky near the cloud edges.

Table 4 shows the results of the retrievals using the three methods. The MOD06 cloud top altitude is derived from the MOD06 cloud top pressure and the radiosonde. The three methods give consistent altitudes and temperatures, even if MOD06 and LaRC techniques show a cloud top above the lidar one (respectively 1.3 and 2.3 km higher). The mean effective cloud altitude given by the LaRC method is 0.8 km above the lidar one (CALIPSO-like). The effective temperature refers to the radiative equivalent temperature of the cloud and is typically below cloud center for optically thin ice clouds. The visible optical thicknesses obtained with the three methods are consistent, ranging between 1.3 and 3. For such a semi-transparent cloud, the CALIPSO-like method uses the lidar-based optical thickness, which is corrected for multiple scattering following Platt (1973) using $\eta=0.5$ (where η is the ratio of apparent visible extinction coefficient to true visible extinction coefficient). The particle effective radii are also consistent varying between, but the CALIPSO-like method gives a smaller result. The MOD06 and CALIPSO-like methods give a larger variability (respectively 23 and 16 μm) than the LaRC technique (9 μm).

B) All SARTA cases

All the 18 SARTA cases are studied as the 8 October 2002 case.

Before any interpretation, it is necessary to note that the MOD06 altitudes and temperatures given in Table 3 do not use the same sample of pixels than all the other products. One consequence is

that for 5 cases, MOD06 technique does not detect any ice cloud using the 5x5 pixels sample (the one used for altitude and temperature retrievals) whereas there is an ice cloud using the pixels strip sample (the one used for the other retrievals: optical depth, effective radius, liquid/ice water path). Figure 2 is the MOD06 optical thickness retrieved from the 5x5 pixels sample, against the one retrieved from the pixels strip sample, when both lead to ice cloud. For 3 cases out of 6, the result is different and illustrates the variability that must be taken into account when we compare cloud temperature and altitude from the different methods.

For two cases (2 April and 14 October 2002) in Table 3, the LaRC and MOD06 effective cloud altitudes are respectively similar and greater than the cloud top detected by the lidar, with consistent cloud top temperatures. For those cases, the optical thicknesses determined with the LaRC and MOD06 methods are greater than the lidar values. In particular, for the 14 October case, the LaRC and MOD06 methods yield $\tau_{\text{LaRC/MOD06}} = 11$ and 11.5 respectively, compared to only 1-3 from the lidar. For those large values of optical thickness, the lidar cannot detect the cloud top. Hence, the CALIPSO-like particle size retrieval is not reliable for those 2 cases. This limitation of CALIPSO-like method to cases where $\tau < 3$ is important for ground base applications but will not be as crucial for future spatial observations, as both lidar and infrared radiometer will be down-looking allowing for the studying of upper cloud layer properties.

In all cases, the CALIPSO-like method detects ice clouds only. For six cases in 2003 (19 and 24 February, 27 March, 15 September, 6 November and 9 December), the cloud is too thin for the MOD06 method to detect clouds along the wind strips. The same thing is observed for 4 cases using LaRC method (19 February, 27 March, 15 September, and 6 November). Those days were selected specifically because the lidar detects subvisible ice clouds with optical thicknesses smaller than 0.2. The 10 remaining cases are used to compare cloud altitude, optical thickness and effective radius. The clouds are identified as mixed water and ice by LaRC method in nine instances, and by MOD06 in three instances, whereas the clouds are only ice from the CALIPSO-like method. Examination of

the imagery reveals that low level clouds are present in the vicinity for the 1st and 8 October and could easily have been included in the pixel strips because of the parallax and advection corrections, which would not be properly applied for low clouds. No low clouds were evident for the 9 December case, which mostly consisted of contrails. For the 6 November 2002 case, the LaRC method retrieves both ice and water clouds. The imagery (not shown) reveals the presence of an extensive, broken low cloud deck. The “comments” column of Table 3 indicates when the LaRC and MOD06 methods find several ice or water pixels, meaning that the pixels composing the strip are classified as ice and liquid phases (a single pixel being associated to one phase only).

Comparisons for the ten scenes where the lidar optical thickness exceeds 0.3 are shown in Figs. 2-5. Figure 3a shows the scatter plot of cloud temperature retrieved with CALIPSO-like method ($T_{\text{CAL-like}}$), as a function of the LaRC retrieved temperature method (T_{LaRC}). In the graph, the variability is the difference between the cloud top and bottom, and the LaRC cloud effective temperature is the cross on errorbars. Figure 3d is the probability density function of the difference between CALIPSO-like and LaRC cloud temperatures. Those two figures show that $T_{\text{CAL-like}}$ is always less than T_{LaRC} , even if they are very close for cases when the CALIPSO-like optical thickness ($\tau_{\text{CAL-like}}$) ranges from 0.8 to 1. Figure 3d shows that for 75% of cases, the difference between $T_{\text{CAL-like}}$ and T_{LaRC} is larger than 20 K and for 25%, the difference is between 0 and 20 K. The greatest difference, 35 K, occurred 9 September 2003 associated with a sub-visible cloud with $\tau_{\text{CAL-like}}$ ranging between 0.09 and 0.1 (Table 3). Figure 3b is the comparison between the CALIPSO-like temperatures and the MOD06 ones when MOD06 using the 5x5 pixels sample finds an ice cloud. As the MOD06 are only available concerning the cloud top, their variability are a standard deviation calculated in the sample. We must compare them with the lowest point of CALIPSO-like errorbars: it shows that the agreement is very good, even if $T_{\text{CAL-like}}$ is most of the time (70%) greater than T_{MOD06} as shown by Figure 3e. The comparison between T_{MOD06} and T_{LaRC} (Figure 3c and f) is

consistent with the other ones: T_{LaRC} is always warmer than T_{MOD06} , showing that the CO₂ slicing technique used for the MOD06 method is more performing.

The results for altitudes (Figure 4) are consistent with the ones obtained for temperatures: for most of the cases, $z_{\text{CAL-like}}$ is greater than z_{LaRC} , except for one case, in which $T_{\text{CAL-like}} = T_{\text{LaRC}}$ (5 March 2002). The greatest difference between $z_{\text{CAL-like}}$ and z_{LaRC} is 6.5 km and corresponds to 17 November 2003, when $\tau_{\text{CAL-like}}$ varied from 0.05 to 1. As for the temperature, the agreement is better between CALIPSO-like and MOD06 methods.

Figure 5a shows the variations of $T_{\text{CAL-like}} - T_{\text{LaRC}}$ as a function of $\tau_{\text{CAL-like}}$. T_{MOD06} and z_{MOD06} are not considered here because of the too few cases where MOD06 detects an ice cloud using the 5x5 pixels sample. The difference between the temperatures and altitudes (Figure 5b) generally decreases as $\tau_{\text{CAL-like}}$ increases. The vertical variability is the difference between the cloud top and bottom from CALIPSO-like method added to standard deviation from LaRC method.

Figure 6 shows the comparison between the optical thicknesses without the two cases with clouds too thick for the CALIPSO-like retrieval. All the other cases are considered in these statistics, even the ones where LaRC and MOD06 methods do not detect any cloud, i.e. when $\tau_{\text{LaRC/MOD06}} = 0$. Figure 6a, b and c show that there is good agreement between the 3 methods for the cases that are not too thick for the CALIPSO-like method and not too thin for LaRC and MOD06 methods, typically meaning $\tau = 0.5-3$. Nevertheless, for 4 thin cases, $\tau_{\text{CAL-like}}$ is smaller than τ_{LaRC} and τ_{MOD06} . This is certainly due to a collocation problem: $\tau_{\text{CAL-like}}$ is calculated using lidar so only for the point above the SIRTa; τ_{LaRC} and τ_{MOD06} are calculated using the strip of pixels that could include a few pixels of a thick cloud, leading to larger values of optical thicknesses. Figure 6d shows that the difference between $\tau_{\text{CAL-like}}$ and τ_{LaRC} is less than 0.2 for 50% of the cases, a result similar to the difference between $\tau_{\text{CAL-like}}$ and τ_{MOD06} (Figure 6e). Nevertheless, $\tau_{\text{CAL-like}}$ is smaller than τ_{MOD06} in 45% of the cases. There is also a good agreement between τ_{LaRC} and τ_{MOD06} in 45% of the cases (difference smaller than 0.2). Overall, τ_{MOD06} tends to be larger than τ_{LaRC} .

Figure 7 summarizes the results for the ice particle effective radius. Figure 7a, b and c show that while there is generally good agreement between the 3 methods, the variability of CALIPSO-like effective radius ($r_{e,CAL-like}$) is often larger than that for either LaRC ($r_{e,LaRC}$) or MOD06 ($r_{e,MOD06}$). The variability difference is probably a result of the differences in the microphysical models used for the retrievals. The CALIPSO-like and LaRC methods have the best agreement: in 60% of the cases, the difference between mean values of $r_{e,CAL-like}$ and $r_{e,LaRC}$ is less than 3 μm (2 main peaks). In 35% of the cases, $r_{e,CAL-like}$ is at least 5 μm larger than $r_{e,LaRC}$. This difference can be very important, in particular for 5 March 2002 case where one can only know that $r_{e,CAL-like}$ is greater than 14 μm . The comparison between $r_{e,CAL-like}$ and $r_{e,MOD06}$ (Figure 7b and e) is similar, but the differences are slightly greater: for 45% of the cases, $r_{e,CAL-like}$ is at least 5 μm smaller than $r_{e,MOD06}$. For 85% of cases, $r_{e,MOD06}$ larger than $r_{e,LaRC}$ and this difference is at least 5 μm for 75% of cases (Figure 7c).

4. Tropical ice clouds during CRYSTAL-FACE field experiment

a. Observations: instruments and dates

Ice cloud observations collected during CRYSTAL-FACE in July 2002 are used to evaluate the CALIPSO-like method in the Tropics.

1) *Airborne 532-nm lidar*. The CPL (Cloud Physics Lidar) is a Nd: YV04 laser. It was nadir-viewing onboard the high altitude NASA ER-2 aircraft, and measures both the backscattered signal at 532 nm and the linear depolarization ratio at 1064 nm. The temporal resolution is 1 Hz, and its vertical resolution is 30 m. For the current study, cloud-base and -top altitudes and the number of cloud layers are from the CPL archived files (<http://cpl.gsfc.nasa.gov/>). The CPL cloud temperatures were found by comparing the cloud base and height data with vertical profiles from the ER-2 dropsondes. The crystal shape information is based on analysis of the lidar depolarization data following the methodology of Noel et al. (2002).

2) *Satellite-borne imager*. The 4-km GOES-8 imager provided observations every 10-15 minutes enabling relatively close matches with the aircraft data. The GOES-8 data were analyzed with the LaRC method (Table 2) using hourly temperature profiles from the Rapid Update Cycle analyses. The retrieved pixel-level cloud properties were averaged for groups of the 4 closest pixels to a point on ER-2 flight track.

3) *An airborne spectrometer*. The MAS instrument flown on the NASA ER-2 aircraft has similar capability as the MODIS instrument; although with much higher spatial resolution (50 m) and more complete spectral coverage provided by grating spectrometers (50 spectral bands). The MAS data are used for both the MAS retrieval and CALIPSO-like methods using a strip of pixels that is 3 pixels (150 m) in the across-track direction, along the length of the selected flight leg. The cloud properties are retrieved for each pixel and then averaged together over the flight leg. The MAS retrieval has similarities to the MOD06 retrieval as previously described, especially in its use of the 2.1 μm band for the primary particle size retrieval.

4) *ER-2 Dropsondes*. These dropsondes are an automated version of the NCAR Airborne Vertical Atmospheric Profiling System (AAVAPS) produced by Vaisala and launched from the ER-2. Details pertaining to the AAVAPS characteristics and performance are described in Hock and Franklin (1999). The AAVAPS provides measurements of pressure, temperature, humidity, and horizontal wind. The sampling rates are 0.5 and 1 Hz for thermodynamic and wind data, respectively. From an ejection altitude of 24 km, the dropsonde requires about 22 minutes to descend to the ocean surface. Between 5 and 6 dropsondes were released during each ER-2 flight. Dropsondes are not available for 29 July flight; hence for this day, data taken by the Balloon Borne Sounding System (BBSS) launched from the Key West ground station (25° N, 81° W) were used.

5) *In-situ measurements*. Hydrometeor size spectra built from combined datasets taken by the CAPS (Cloud, Aerosols, and Precipitation Spectrometer), CPI (Cloud Particle Imager), and SPP-100 optical spectrometer on the WB-57 aircraft are used to evaluate the remote sensing techniques. The CAPS measures ice particle diameter over two ranges, 0.5 - 44 μm and 75 - 1600 μm (Baumgardner et al., 2001); the SPP-100 measures between 4 and 60 μm , while the CPI covers 10 - 300 μm . After re-binning each measurement, an average concentration is computed for each overlapping effective size bin. The particle volume and cross sectional area were computed from the size distributions with the assumption that the particles were ice spheres with density 0.9. Both parameters will be overestimated since recent studies (Baumgardner et al., 2005) show that the cirrus particles in CRYSTAL-FACE had shapes that are representative of ensembles of bullet rosettes, plates and hollow columns. All of these habits have equivalent volumes less than a sphere. The uncertainty in volume is approximately $\pm 50\%$, based on comparisons of different habits with equivalent spheres. We estimate the uncertainty in area as approximately $\pm 30\%$ since the cross sectional areas of rosettes, columns and plates are much more similar to those of spheres with the same equivalent diameter. The uncertainties in volume and area are correlated; hence, error propagated into the calculation of effective radius is approximately $\pm 40\%$.

Collocated ER-2 and WB-57 aircraft data were determined using navigational recorder data provided by K. Drdla (also available at http://www.espoarchive.nasa.gov/cgi-bin/dl_start). The ER-2 and WB-57 data are considered to be coincident when the planes pass the same location within ± 5 minutes.

The cases were selected using almost the same criteria as in mid-latitudes (Sect. 3.b). The main difference is that for CRYSTAL-FACE, each case corresponds to a flight leg instead of a day, and several flight legs are studied in a given day. Using the CPL information, a flight leg is selected when the cloud has relatively constant (± 150 m) bottom and top altitudes so that a single IR

radiative transfer computation can be used for the entire flight leg to apply the CALIPSO-like method. The lidar depolarization is used to select ice cloud in flight legs. For those cases, the CALIPSO-like method is not limited to cases where $\tau < 3$ because both the imager (MAS or GOES) and lidar (CPL) are down-viewing. Nevertheless, other limitations of this method will be demonstrated. A total of 14 different flight legs were analyzed. Particle effective radii and optical thickness were retrieved for each pixel and then averaged along the flight leg. Table 5 summarizes the dates and time periods of observations for the different instruments, and the altitudes of each cloud.

b. Comparison of the three methods

A) Illustrative case: flight leg 8

Figure 8a shows the temporal and altitude variation of the CPL lidar depolarization ratio. It indicates that the cloud top altitude varies between 15 and 11 km. Around 2217 UTC (red arrow), the cloud top altitude is constant, and the depolarization ratio ranges between 30% and 50% within the cloud, indicating that it is an ice cloud. Figure 8b shows the GOES visible image at this time together with the ER-2 plane flight track. The rise in the cloud-top around 2211 UTC is evident as a shadow line in the visible image. At 2217 UTC, the ER-2 is over the ocean, making this flight leg a good case study because the surface albedo is low. Figure 8b shows that the plane crosses the edge of a cumulonimbus anvil at the end of the flight leg (blue and magenta line segments). For this flight leg, the LaRC method classified most of the pixels as ice except for a few pixels that were defined as liquid water or clear. The MAS and CALIPSO-like techniques classified all of the pixels as ice clouds. This difference is likely due to the large discrepancies in spatial resolutions between the LaRC method using GOES data (8-km resolution across and 4-km resolution along the flight leg) and CALIPSO-like and MAS methods using MAS data (150 m resolution along the flight leg). The patterns in optical thickness seen in the MAS (Fig. 6c) and GOES (Fig. 6d) results are generally

consistent over the relatively short length of the flight leg. The ice cloud optical thickness is often larger than 3 in anvils; hence for the CALIPSO-like method, the cloud optical thickness is determined in the IR by comparing the radiative transfer computations with the measured radiance. This was not the case for the SIRTa study where the optical thickness was determined from lidar because clouds were semi-transparent.

Table 6 summarizes the results obtained with the 3 methods for flight leg 8. Both passive remote sensing techniques underestimate the cloud altitude as detected by the lidar: The LaRC method locates the cloud between 4.5 km below to 0.5 km above cloud base, whereas the MAS method identifies it just below the cloud base. Similarly, T_{LaRC} is ~ 27 K greater than $T_{\text{CAL-like}}$. Hence, both passive methods miss the highest part of the cloud, whereas the CALIPSO-like method misses the lower part of the cloud where the lidar cannot penetrate. This result is consistent with the analysis of Sherwood et al. (2004) who found that the thermal infrared GOES channel brightness temperatures correspond to an altitude 1- 2 km below the physical top of even the densest cumulonimbus clouds.

Generally, there is a good agreement between the CALIPSO-like method and both passive methods for the optical thicknesses, although the GOES yields a greater maximum value because its large pixels include the bright clouds seen in the lower left-hand corner of the MAS image. These clouds were not included in the narrow strip of MAS and CALIPSO-like retrievals. The three methods yield mean particle effective radii ranging between 22 and 40 μm with variability between 7 and 18 μm depending on the method. The CALIPSO-like method yields the smallest mean value of r_e .

B) All 14 CRYSTAL-FACE flight legs

Table 5 summarizes the results for 14 CRYSTAL-FACE flight legs. LaRC results are reported only for the pixels identified as ice clouds. For 5 flight legs (all three 23 July flight legs, flight leg 7, and flight leg 12), no particle effective radius and optical thickness were retrieved using

the CALIPSO-like method because the measured BTD values were outside the range of the model calculations. Those 5 flight legs correspond to very large values of τ_{LaRC} and τ_{MAS} (Table 5) with a maximum value of τ_{LaRC} equal to 127 (flight leg 12). For such thick clouds, the BTD's measured by MAS in the CALIPSO-like channels have values ranging between -1 and -3.5 K (depending on the spectral interval). Such values cannot be reproduced by simulations, whatever the microphysical properties of the crystals. All those cases correspond to large convective systems as seen in the GOES visible images (not shown). During four of the five flight legs, the lidar depolarization only yields aspect ratio of class I, indicating that the cloud particles are likely to be plates or nearly spherical particles. This class was found in seven other flight legs. For those 5 flight legs, Table 5 shows that the LaRC optical thickness is greater than 11 and the MAS one is greater than 7. It means that the CALIPSO-like method cannot be applied to clouds thicker than $\tau_{\text{LaRC}} = 11$ or $\tau_{\text{MAS}} = 7$. This limitation is a general limitation of the CALIPSO-like technique; it is not the same as the SARTA cases limitation that was only due to the fact that the SARTA lidar was at ground whereas the MODIS instrument was space-board.

For two cases (flight legs 13 and 14) that also correspond to very thick clouds, the CALIPSO-like method was applied to pairs of channels in order to select a particle model for each BTD, but none of the particle models could explain consistently the three different BTD values, hence the particle effective radius could not be retrieved. This is probably because the cloud particles in those flight legs are not represented in any of the CALIPSO-like particle models. Actually, it could correspond to very small non-spherical particles like droxtal that have been observed at the top of anvils. Infrared and visible optical properties computation are not yet available for such crystals, but will be available for the operational version of this method, i.e. for applying it to the CALIPSO instruments. For the 8 cases when $r_{e,\text{CAL-like}}$ could not be retrieved, however, both passive methods produced results. As seen in Figure 9, $r_{e,\text{MAS}}$ greatly exceeds its LaRC counterpart for 5 of those cases, while results from the two methods agree within $\pm 1 \mu\text{m}$ for the other 3 cases.

Results from the three different methods are compared in Figs. 10 - 12 for the other seven flight legs. Figure 10a plots $T_{\text{CAL-like}}$ as a function of T_{LaRC} . Variability is the difference between the cloud top and bottom detected with CPL, whereas the LaRC one is a standard deviation of the cloud effective temperature, calculated in the box of pixels used for the retrieval. Figure 10b shows the probability density function of the difference between $T_{\text{CAL-like}}$ at the cloud middle height and the mean T_{LaRC} . Except for one case, $T_{\text{CAL-like}}$ is always less than T_{LaRC} . Actually, as for flight leg 8 (previous section), the LaRC method often misses the highest (coldest) part of the cloud (cooler) whereas the CALIPSO-like method often misses the lowest (warmest) part of the cloud. Exceptions include the two cases when the lidar detected a midlevel cloud below the cirrus cloud. In those two cases, the optical thickness of the upper cloud was so small that the LaRC technique only detected the lower cloud because T_{LaRC} and the low cloud temperature from CALIPSO-like method are nearly identical (not shown). In 45% of cases, the difference between $T_{\text{CAL-like}}$ and T_{LaRC} is smaller than 10 K. This tendency is confirmed in Figure 10c and d that compare the cloud altitudes retrieved from all 3 methods. In 92% of cases, $z_{\text{CAL-like}}$ is higher than z_{LaRC} , and in one case when the lidar detected two layers, the difference is 7 km. The difference between $z_{\text{CAL-like}}$ and z_{MAS} is smaller: $z_{\text{CAL-like}}$ is larger than z_{MAS} in only 43% of the cases. Otherwise, z_{MAS} is higher than z_{LaRC} all the time, and the difference is larger than 6 km in 45% of cases. For the thin clouds, e.g., the three flight legs of July 26th 2002, the lidar can detect even the thinnest parts of the cloud, as indicated by the range of retrieved optical thicknesses. As seen for the SIRTAs cases, the range of optical thicknesses retrieved by MAS and LaRC tend to be bounded by a greater minimum value than found by the CALIPSO-like approach and the passive method cloud heights are, on the whole, less than the lidar-determined values (Figure 10c).

Figure 11 compares the optical thicknesses obtained with the 3 methods. The difference between τ_{MAS} and τ_{LaRC} is less than 1 for only 12% of cases, and τ_{MAS} is larger than τ_{LaRC} by more than 2 for 50% of cases. As shown in Table 5, this difference is very large for the flight legs without

CALIPSO-like retrievals. Actually, the CALIPSO-like optical thickness cannot be retrieved from the same technique as for SARTA cases because CRYSTAL-FACE clouds are very thick, hence the lidar does not detect the cloud bottom and it is not possible to calculate any lidar optical thickness. Hence, we use the infrared radiances to estimate an infrared optical thickness that is called $\tau_{\text{IR}_{\text{CAL-like}}}$. It cannot be compared directly with the other methods because it is an infrared optical thickness whereas τ_{MAS} and τ_{LaRC} are visible optical thickness. When considering a cloud composed of large particles, the ratio between visible and infrared optical thicknesses is about 2. Actually, Figure 11a and b show that the plot of $\tau_{\text{IR}_{\text{CAL-like}}}$ as a function of τ_{MAS} and τ_{LaRC} is better matched with the $x = 2y$ line than with $x = y$ line, especially for the smallest optical thickness values. Since the CALIPSO-like optical thicknesses for the CRYSTAL-FACE data are based on infrared retrievals, any values exceeding 3 or 4 are highly suspect. The MAS retrieval tends to yield greater optical thicknesses than the LaRC approach.

Figure 12 shows the comparisons between the particle effective radii obtained with the three methods. In only one of those cases where the 3 retrieval methods can be applied, is the effective radius retrieval good (Figure 12a and b). For the other cases, the mean CALIPSO-like retrieval can be twice the LaRC and MAS values. The agreement between the CALIPSO-like and LaRC results is slightly better than that with the MAS method. On average, for the five cases, $r_{e,\text{CAL-like}}$ is 20.5 μm , compared to 11 and 13.5 μm for LaRC and MAS. The differences in r_e for the two passive methods in Figure 12c (37%) are much like those seen in Figure 9 (33%). Table 5 shows that for those 5 flight legs, the lidar depolarization ratios lead to aspect ratios Q in classes I, II, and III, i.e. $Q < 1.1$. With this knowledge, it is difficult to trust the $r_{e,\text{LaRC}}$ retrieval as it only uses column habits, corresponding to $Q > 1.1$. This could explain the large difference between $r_{e,\text{CAL-like}}$ and $r_{e,\text{LaRC}}$ and the smaller differences between $r_{e,\text{CAL-like}}$ and $r_{e,\text{MAS}}$.

c. Comparison with in-situ measurements

The particle effective radius results are compared to In-Situ measurements in Table 7. For the sake of sampling, the WB-57 aircraft is considered to be collocated with the ER-2 if the time difference between the passages of two aircraft over the coincident point (defined in Sect. 4a) is less than 22 minutes. Hence, five flight legs have the WB-57 passing over coincidence points to within 14-22 minutes of the ER-2 flight path. For example, flight leg #12 is at 19.82 UTC for ER2; the coincident point for WB57 is 14 minutes later, i.e. at 20.05 UTC; hence, the averaged value and the standard deviation of $r_{e,In-Situ}$ (Table 7) is estimated using values between 19.97 and 20.13 UTC, i.e. 10 minutes around the coincident point. A value of $r_{e,In-Situ}$ is estimated at each time by calculating $\langle V \rangle$ and $\langle A \rangle$ for the all size distribution, from 0.175 to 800 μm and using Eq. 1. Tests have been done (not shown) by considering the size distribution only from 1.5 to 800 μm in order to know if small particles introduce a bias in the results: it only changes the results by 0.5 μm at the most. Furthermore, we explained in Sect. 4a that the habit hypothesis for In-Situ leads to a $\pm 40\%$ error on the $r_{e,In-Situ}$ calculation. The value of this uncertainty is also presented in Table 7. Only one of those 5 flight legs corresponds to a case with a possible CALIPSO-like retrieval. For this flight leg 8, as noted earlier, the agreement is good between CALIPSO-like, LaRC, and MAS, and the Table shows that it is also in a good agreement with in-situ measurements. Nevertheless, the uncertainty about $r_{e,In-Situ}$ shows that its value can be from 20 to almost 50 μm , so with a large range. Also, the remote observations give a mean effective radius weighted over the vertical extent of the cloud whereas the In-Situ observations are collected at a given altitude of the cloud. Moreover, the coincidence time for this flight leg is 22 minutes, the greatest for the set and that could lead to collocation problem. For other cases (Table 7), the In-Situ particle sizes are still in a very good agreement with the other, in particular with MAS method. They still have a larger range because of the uncertainty, and for leg 12, 13 and 14, they tend to be larger than the LaRC ones. This result is not consistent with the fact that In-Situ measurements are often biased by small particles.

5. Discussion and conclusions

This study intends to compare ice cloud properties derived from the so-called CALIPSO-like method using collocated passive and active remote-sensing observations with two other well known passive imager methods (from the CERES team and the MODIS operational cloud product team). The CALIPSO-like method requires lidar measurements and is most suitable for thin ice clouds. Nevertheless, this method must be validated in different ice cloud conditions (thin and thick) and at different latitudes (mid-latitudes at SIRTa and Tropics in Florida). Figure 13 shows the phase retrieval from the 2 passive remote sensing methods when the lidar algorithm detects an ice cloud (i.e. for all the selected cases). The “liquid water + ice” occurrence means that liquid water and ice are found in the sample of pixels, and not that there is mixed phase. Actually, there is no mixed phase category for LaRC and MOD06/MAS retrievals. The agreement between the 3 methods concerning the detection of ice is better for tropical ice clouds: 70% of tropical clouds are ice for the LaRC method against 50% for mid-latitude clouds, and 84% of tropical clouds are ice for MOD06/MAS method against 45% for mid-latitude clouds. For tropical clouds, 30% are interpreted as ice and water by the LaRC algorithms and 8% by the MOD06/MAS algorithm. Furthermore, for mid-latitude cases, 35% for LaRC algorithms and 30% for MOD06/MAS are classified as clear sky. There is no case interpreted as only water by the LaRC algorithms, whereas 5% at mid-latitude and 8% at tropics are only water for MOD06/MAS. These results confirm the importance of lidar observations for thin ice cloud retrievals, most of which are found at mid-latitudes. The CALIPSO-like technique is then well suited for this kind of cloud, despite its sensitivity to small changes or uncertainties in the brightness temperature of each IR channel used, in particular due to the surface emissivity or the calibration (Chiriaco et al., 2004).

When the retrieval is possible, the comparison between ice particle effective radii obtained with the three methods give encouraging results keeping in mind that the three methods are based on different approaches and are using different wavelengths. At mid-latitudes, the lidar is on the ground and the Spectroradiometer in space, so the CALIPSO-like method has been applied to clouds with

optical thicknesses less than 3, in order to be sure that both instruments are sensing the same cloud. Considering such clouds, and also thick enough for being detected by passive remote sensing methods, the agreement between the three methods is quite good for r_e retrieval, independently of the quality of the cloud altitude and temperature retrieval. CALIPSO-like and LaRC methods have the best agreement for r_e at mid-latitude: in 50% of the cases, the difference between $r_{e,CAL-like}$ and $r_{e,LaRC}$ is less than 3 μm , and $r_{e,CAL-like}$ is at least 5 μm larger than $r_{e,MOD06}$. In the tropics, CALIPSO-like method can only be applied to a few cases, also leading to a relatively good agreement between the 3 methods: in 40% of cases, the difference between $r_{e,CAL-like}$ and $r_{e,LaRC}$ or $r_{e,MAS}$ is less than 3 μm , and $r_{e,CAL-like}$ seems to overestimate $r_{e,LaRC}$ and $r_{e,MAS}$ in 40% of cases. In the tropics, there are often large differences between $r_{e,CAL-like}$ and the two other methods: those cases correspond to cloud with a microphysics that is not taken into account in LaRC and MAS methods (typically plates, as shown by the lidar depolarisation ratio). Furthermore, there is a good agreement between $r_{e,LaRC}$ and $r_{e,MOD06}$ when the cloud optical thickness is moderate, whereas there is a strong discrepancy in very thick clouds for which CALIPSO-like method did not give any results. Hence, it seems that whatever the method used, the estimation of the particle effective radius in strongly convective clouds in the tropics remains a challenging task. One important conclusion concerning the particle size retrieval is the complementary role between the different methods: the lidar method is powerful for thin clouds but not for thick clouds, and vice-versa for the passive methods.

This study contributes to quantify the limits of the CALIPSO-like method. The method can contribute to improve the knowledge of thin and subvisible clouds properties where passive methods are less reliable. Currently the CALIPSO-like method cannot be applied to derive particle effective radius and optical thickness in very thick ice clouds in the tropics because the theoretical radiative computation used for this method are unable to reproduce negative BTDs above thick cold ice clouds as seen in the observations. Several theoretical scenarios (Chepfer et al. submitted) have been studied to explain this discrepancy such as including large variability in the temperature profile around the

tropopause level, or different microphysical models, leading to the conclusion that CALIPSO-like method using MODIS data fails in presence of nitric acid in ice clouds that is not taken into account in the radiative transfer computations. The CALIPSO-like method applied to the real IIR/CALIPSO channels that are slightly different of the MODIS ones should give much better results for those cases because not influenced by nitric acid absorption.

Future work will consist in applying the CALIPSO-like method to space-borne observations. This will cover a large dataset in various latitude and time periods. The retrieval will be validated against in-situ data as well as ground-based retrievals and other satellite retrievals.

Acknowledgments

The GOES analyses were supported by the NASA Radiation Sciences Branch through the CRYSTAL-FACE project. The LaRC MODIS analyses were supported by the NASA Earth Sciences Program through the LaRC Project. The authors acknowledge SIRTa for providing the ground-based lidar data.

References

- Ackerman, T., and G. Stokes (2003), The Atmospheric Radiation Measurement Program, *Physics Today*, **56**, 38 – 45.
- Ackerman, S. A., K. I. Strabala, W. P. Menzel, R. A. Frey, C. C. Moeller and L. E. Gumley, 1998: Discriminating clear-sky from clouds with MODIS. *J. Geophys. Res.*, **103**, 32141-32158.
- Baum, B. A., P. F. Soulen, K. I. Strabala, M. D. King, S. A. Ackerman, W. P. Menzel, and P. Yang, 2000b: Remote sensing of cloud properties using MODIS Airborne Simulator imagery during SUCCESS. II. Cloud thermodynamic phase. *J. Geophys. Res.*, **105**, 11,781-11,792.
- Baumgardner, D., H. Jonsson, W. Dawson, D. O'Connor and R. Newton, 2001: The cloud, aerosol and precipitation spectrometer (CAPS): A new instrument for cloud investigations, *Atmos. Res.*, **59-60**, 251-264.
- Baumgardner, D., H. Chepfer, G.B. Raga and G.L. Kok, 2005: The Shapes of Very Small Cirrus Particles Derived from In Situ Measurements, *Geophys. Res. Lett.*, **32**, L01806, doi:10.1029/2004GL021300, 2005
- Chakrapani, V., D. R. Doelling, A. D. Rapp, and P. Minnis, 2002: Cloud thickness estimation from GOES-8 satellite data over the ARM SGP site. *Proc. 12th ARM Science Team Meeting*, April 8-12, St. Petersburg, FL, 14 pp. Available at http://www.arm.gov/docs/documents/technical/conf_0204/chakrapani-v.pdf.
- Chepfer H., P. Dubuisson, M. Chiriaco, P. Minnis, S. Sun-Mack and E. D. Riviere: Negative brightness temperature (11-12 μm) in Cold Thick Ice Clouds: A Signature of Nitric Acid. *Submitted to the J. of Geophys. Res.*
- Chiriaco M., H. Chepfer, V. Noël, A. Delaval, M. Haeffelin, P. Dubuisson and P. Yang, 2004: Improving retrievals of cirrus cloud particle size coupling lidar and 3-channels radiometric Techniques. *Mon. Wea. Rev.*, **132**, 1684-1700.

- Derber, J. C., D. F. Parrish and S. J. Lord, 1991: The new global operational analysis system at the National Meteorological Center. *Weather Forecasting*, **6**, 538-547.
- Dubuisson, P., V. Giraud, O. Chomette, H. Chepfer and J. Pelon, 2005: Fast Radiative Transfer Modeling for Infrared Imaging Radiometry. *J. Quant. Spectrosc. Radiat. Transfer*, In press.
- Haefelin, M., L. Barthès, O. Bock, C. Boitel, S. Bony, D. Bouniol, H. Chepfer, M. Chiriaco, J. Cuesta, J. Delanoë, P. Drobinski, J-L. Dufresne, C. Flamant, M. Grall, A. Hodzic, F. Hourdin, F. Lapouge, Y. Lemaître, A. Mathieu, Y. Morille, C. Naud, V. Noël, B. O'Hirok, J. Pelon, C. Pietras, A. Protat, B. Romand, G. Scialom and R. Vautard, 2005: SIRTa, a ground-based atmospheric observatory for cloud and aerosol research. *Annales Geophysicae*, **23**, pp 253-275.
- Heymsfield, A. J., 1975: Cirrus uncinus generating cells and the evolution of cirriform clouds. Part I: Aircraft observations of the growth of the ice phase. *J. Atmos. Sci.*, **32**, 799-807.
- Heymsfield, A. J., and C. M. R. Platt, 1984: A parameterization of the particle size spectrum of ice clouds in terms of the ambient temperature and the ice water content. *J. Atmos. Sci.*, **41**, 846-855.
- Heymsfield, A.J., 1993: Microphysical Structure of Stratiform and Cirrus Clouds. *Aerosol Cloud Climate Interactions. P. V. Hobbs, Ed.*, **54** in the International Geophysics Series, 233pp.
- Hock, T. F., J. L. Franklin, 1999: The NCAR GPS dropwindsonde. *Bull. of the Am. Meteorol. Soc.*, **80**, 407-420.
- Intrieri J., G. L. Stephens, W. L. Eberhard, and T. Uttal, 1993: A method for determining cirrus cloud particles size using lidar and radar backscatter technique. *J. Appl. Meteorol.*, 1074-1082.
- Intrieri J. M., W. L. Eberhard, T. Uttal, J. A. Shaw, J. B. Snider, Y. Han, B. W. Orr, and S. Y. Matrosov, 1995: Multiwavelength observations of a developing cloud system: the FIRE II 26 November 1991 case study. *J. Atmos. Sci.*, **52**, 4079-4093.
- Jensen, E., D. Starr, and O. B. Toon, 2004: Mission investigates tropical cirrus clouds. *EOS*, **85**, 45-50.

- King, M. D., W. P. Menzel, Y. J. Kaufman, D. Tanre, B. C. Gao, S. Platnick, S. A. Ackerman, L. A. Remer, R. Pincus, and P. A. Hubanks, 2003: Cloud and aerosol properties, precipitable water, and profiles of temperature and humidity from MODIS. *IEEE Trans. Geosci. Remote Sens.*, **41**, 442-458.
- King, M. D., S. Platnick, P. Yang, G. T. Arnold, M. A. Gray, J. C. Riedi, S. A. Ackerman, K. N. Liou, 2004: Remote sensing of liquid water and ice cloud optical thickness and effective radius in the Arctic: Application of airborne multispectral MAS data. *J. Atmos. Oceanic Tech.*, **21**, 857-875.
- Krupp, C., 1991: Holographic measurements of ice crystals in cirrus clouds during the International Cloud Experiment ICE 1989. In *Report of the 4th ICE/EUCREX Workshop*, Laboratoire d'Optique Atmosphérique, USTL, Lille, France.
- Liou, K. N., 1986: Influence of cirrus clouds on weather and climate processes: A global perspective. *Mon. Wea. Rev.*, **114**, 1167-1199.
- McFarquhar, G. M., P. Yang, A. Macke, and A. J. Baran, 2002: A new parameterization of single-scattering solar radiative properties for tropical anvils using observed ice crystal size and shape distributions. *J. Atmos. Sci.*, **59**, 2458-2478.
- Mace G. G., K. Sassen, S. Kinne, T. P. Ackerman, 1998: An examination of cirrus cloud characteristics using data from millimeter wave radar and lidar: The 24 April SUCCESS case study. *Geophys. Res. Lett.*, **25**, 1133-1136.
- Mace, G. G., Y. Zhang, S. Platnick, M. D. King, P. Minnis, and P. Yang, 2004: Evaluation of cirrus cloud properties from MODIS radiances using cloud properties derived from ground-based data collected at the ARM SGP site. In press, *J. Appl. Meteorol.*
- Macke, A., J. Mueller and E. Raschke, 1996: Single scattering properties of atmospheric ice crystals. *J. Atmos. Sci.*, **53**, 2813-2825.

- Matrosov S. Y., 1999: Retrievals of vertical profiles of ice cloud microphysics from radar and IR measurements using tuned regressions between reflectivity and cloud parameters. *J. Geophys. Res.*, **104**, 16,741-16,753.
- McFarquhar, G.M., and A. J. Heymsfield, 1996: Microphysical characteristics of three anvils sampled during the Central Equatorial Pacific Experiment. *J. Atmos. Sci.*, **53**, 2401-2423.
- Menzel, W. P., W. L. Smith and T. R. Stewart, 1983: Improved cloud motion wind vector and altitude assignment using VAS. *J. Appl. Meteorol.*, **22**, 377-384.
- Minnis, P., D. P. Kratz, J. A. Coakley, Jr., M. D. King, D. Garber, P. Heck, S. Mayor, D. F. Young and R. Arduini, 1995: Cloud Optical Property Retrieval (Subsystem 4.3). Clouds and the Earth's Radiant Energy System (CERES) algorithm theoretical basis document, Volume III: Cloud Analyses and Radiance Inversions (Subsystem 4). *NASA RP 1376*, Vol. 3, 135-176.
- Minnis, P., D. P. Garber and D. F. Young, 1998: Parameterizations of reflectance and effective emittance for satellite remote sensing of cloud properties. *J. Atmos. Sci.*, **55**, 3313-3339.
- Minnis, P., L. Nguyen, W. L. Smith, Jr., M. M. Khaiyer, R. Palikonda, D. A. Spangenberg, D. R. Doelling, D. Phan, G. D. Nowicki, P. W. Heck, and C. Wolff, 2004: Real-time cloud, radiation, and aircraft icing parameters from GOES over the USA. *Proc. 13th AMS Conf. Satellite Oceanogr. and Meteorol.*, Norfolk, VA, Sept. 20-24, CD-ROM, P7.1.
- Minnis, P., D. F. Young, S. Sun-Mack, P. W. Heck, D. R. Doelling, and Q. Z. Trepte, 2003: CERES cloud property retrievals from imagers on TRMM, Terra, and Aqua. *SPIE 10th Intl. Symp Remote Sens., Conf. Remote Sens. Clouds and Atmos.*, Barcelona, Spain, September 8-12, 37-48.
- Noel, V., H. Chepfer, G. Ledanois, A. Delaval, and P. H. Flamant, 2002: Classification of particle effective shape ratios in cirrus clouds based on lidar depolarization ratio. *Appl. Opt.*, **41**, 4245-4257.
- Pilewskie, P. and S. Twomey, 1987: Discrimination of ice from water in clouds by optical remote sensing. *Atmos. Res.*, **21**, 113-122.

- Platnick, S. M. D. King, H. Gerber and P. V. Hobbs, 2001: A solar reflectance technique for cloud retrievals over snow and ice surfaces. *J. Geophys. Res.*, **106**, 15,185-15,199.
- Platnick, S., M. D. King, S. A. Ackerman, W. P. Menzel, B. A. Baum, J. C. Riedi and R. A. Frey, 2003: The MODIS cloud products: Algorithms and examples from Terra. *IEEE Trans. Geosci. Remote Sens.*, **41**, 459-473.
- Platt C. M. R., 1973: Lidar and radiometric observations of cirrus clouds. *J. Atmos. Sci.*, **30**, 1191-1204.
- Platt C. M. R., J. D. Spinhirne, and W. D. Hart, 1989: Optical and microphysical properties of a cold cirrus cloud: Evidence for regions of small particles. *J. Geophys. Res.*, **94**, 11151-11164.
- Randall, D., B. Albrecht, S. Cox, D. Johnson, P. Minnis, W. Rossow, and D. Starr, 1996: On FIRE at ten. *Adv. Geophys.*, **38**, 37-177.
- Raschke, E., P. H. Flamant, Y. Fouquart, P. Hignett, H. Hisaka, P.R. Jonas, H. Sundquist and P. Wendling, 1998: Cloud-radiation studies during the European Cloud Radiation Experiment (EUCREX). *Surveys in Geophys.*, **19**, 89-138.
- Raschke, E., J. Schmetz, J. Heitzenberg, R. Kandel, and R. Saunders, 1990: The International Cirrus Experiment (ICE): A joint European effort. *ESA Journal*, **14**, 199-.
- Sherwood, S. C., J.-H. Chae, P. Minnis, and M. McGill, 2004: Underestimation of deep convective cloud tops by thermal imagery. *Geophys. Res. Lett.*, **31** (11), 10.1029/2004GL019699.
- Takano, Y. and K. N. Liou, 1989: Solar radiative transfer in cirrus clouds. Part 1: Single-scattering and optical properties of hexagonal ice crystals. *J. Atmos. Sci.*, **46**, 3-18.
- Toon, O. B. and R. C. Miake-Lye, 1998: Contrails and cloud Effects Special Study (SUCCESS). *Geophys. Res. Lett.*, **25**, 1109-1112.
- Trepte, Q., P. Minnis and R. F. Arduini, 2002: Daytime and Nighttime Polar Cloud and Snow Identification using MODIS data. *Proc. SPIE3rd intl. Asia-Pacific Environ. Remote Sensing*

Symp. 2002: Remote Sens. of Atmosphere, Ocean, Environment, and Space, Hangzhou, China, October 23-27, Vol 4891, 449 – 459.

Wendling, P., R. Wendling and H. K. Weickmann, 1979: Scattering of solar radiation by hexagonal ice crystals. *Appl. Opt.*, **18**, 2663-2671.

Winker, D. M., J. Pelon and M. P. McCormick, 2003 : The CALIPSO mission: Spaceborne lidar for observation of aerosols and clouds, *SPIE Asia-Pacific Symposium on Remote Sensing of the Atmosphere, Environment and Space*, Hangzhou, China, 23-27 October, 4893-01.

Yang, P. and K. N. Liou, 1996: Finite-difference time domain method for light scattering by small ice crystals in three-dimensional space. *J. Opt. Soc. Amer*, **13**, 2072-2085.

Yang, P. and K. N. Liou, 1996: Geometric optics integral equation method for light scattering by nonspherical ice crystals. *Appl. Opt.*, **35**, 6568-6584.

Yang, P., B. Gao, B. A. Baum, Y. X. Hu, W. J. Wiscombe, S. Tsay and D. M. Winker, 2001: Radiative properties of cirrus clouds in the infrared (8-13 μ m) spectral region, *J. Quant. Spectr. & Rad. Trans.*, **70**, 473-504.

Young, A.T., 1980: Revised depolarization corrections for atmospheric extinction. *Appl. Opt.*, **19**, 3427-3428.

Young, D. F., P. Minnis, D. Baumgardner, and H. Gerber, 1998: Comparison of in situ and satellite-derived cloud properties during SUCCESS. *Geophys. Res. Lett.*, **25**, 1125-1128.

Table captions

Table 1: Cloud properties retrieved from 3 methods

Table 2: Spectroradiometers and sampling used for each method

Table 3: Mid-latitude ice clouds case. (1): ground temperature from SIRTAs instruments. “b” subscript is “base”, “T” subscript is “Top”, “e” subscript is “effective”.

Table 4: Results of the three retrieval methods for 8 October 2002 case.

Table 5: Tropical ice clouds cases during CRYSTAL-FACE.

Table 6: Results of the three retrieval methods for flight leg 8, mean with range in parentheses.

Table 7: Comparison between re,In-Situ averaged over 10 minutes, re,CAL-like, re,LaRC, and re,MAS for the 5 flight legs with coincidence between the ER-2 and WB-57 flight paths.

Table 1: Cloud properties retrieved from 3 methods

	pha	T_{top}	T_{eff}	Z_{top}	Z_{eff}	P_{top}	P_{bot}	P_{eff}	τ	LWP	$r_{\text{e,ice}}$	layers
	se	T_{bot}		Z_{bot}						IWP	$r_{\text{e,wat}}$	
CALIPSO-												
like	x	x	x	x	x	x	x	x	x		x	x
LaRC	x	x	x	x	x	x	x	x	x	x	x	
MOD06												
(SIRTA)	x	x				x			x	x	x	
MAS												
(CRYSTAL)	x					x			x	x	x	x

Table 2: Spectroradiometers and sampling used for each method

	CALIPSO-like method/<u>SIRTA</u>	LaRC method/<u>SIRTA</u>	MOD06 method/<u>SIRTA</u>
instruments	MODIS/SIRTA lidar	MODIS	MODIS
channels	8.65, 11.15, 12.05 μm	0.65, 3.75, 10.8, 12.05 μm	20 bands from visible to infrared
sampling	pixel strip 3-km wide \pm 1 h around <i>Terra</i> overpass	pixel strip 3-km wide \pm 1 h around <i>Terra</i> overpass	- pixel strip 3-km wide \pm 1 h around <i>Terra</i> overpass - 5x5 pixels area (5x5 km ²) centred on the SIRTA (for cloud top pressure and temperature retrievals)
	CALIPSO-like method/<u>CRYSTAL- FACE</u>	LaRC method/<u>CRYSTAL-FACE</u>	MAS method/<u>CRYSTAL-FACE</u>
instruments	ER-2 MAS/cloud lidar	GOES-8 imager	ER-2 MAS
channels	8.4, 10.8, 12.0 μm	0.65, 3.9, 10.8, 12 μm	20 bands from visible to infrared
sampling	3x3 pixel array (150X150 m ²) nadir over length of flight leg	Mean retrievals from 4x4 4-km pixel arrays along ER-2 flight leg	3x3 pixel array (150X150 m ²) nadir over length of flight leg

Table 3: Mid-latitude ice clouds case. (1): ground temperature from SARTA instruments. “b” subscript is “base”, “T” subscript is “Top”, “e” subscript is “effective”.

Date	UTC	Skin Temp (K)	CALIPSO-like			LaRC		MOD06		Comments
			Z _b (km) T _b (K)	Z _T (km) T _T (K)	τ_{lidar}	z _e , (km) T _e (K)	τ_{ice}	z _T , (km) T _T (K)	τ_{ice}	
5/3/02*	1110	281	7.3 234	9.5 214	0.8-1	7.7 238	0.8	9.9 217	1.4	LaRC: 2 ice layers MOD06: ice
2/4/02	1045	290	7 242	9.2 225	1.5-2	9.2 226	2.9	10.4 215	3	CALIPSO-like: cloud top not detected LaRC: 2 ice layers MOD06: ice
1/10/02*	1055	290	8.8 236	10.7 219	1-4	8.8 235	2.2	10.1 225	2.6	LaRC: ice and liquid water MOD06: ice
8/10/02*	1105	285	6.1 251	11 214	1.4-3	7 244	1.8	9.7 222	2.2	LaRC: ice and liquid water MOD06: ice
14/10/02	1210	285	5.5 259	8 241	1-3	10.2 224	11	No cloud	11	CALIPSO-like: cloud top not detected LaRC: ice MOD06: ice
6/11/02*	1030	282	6.9 247	10.7 222	0.4-1.2	6.3 250	2.4	10.9 217	3.2	LaRC: ice and liquid water MOD06: ice
19/12/02*	1015	273	8.6 230	12 202	0.8-1.2	6.8 239	0.9	10.4 214	1.3	LaRC: 2 ice layers MOD06: ice
19/12/02	1150	274	10.3 216	11.9 202	0.2-0.3	6.8 235	0.3	No cloud	1	LaRC: 4 ice layers MOD06:
19/2/03	1025	271	8.8 223	10.2 211	0.2	No ice		No ice		LaRC: liquid water MOD06: liquid water
24/2/03	1040	283	7.5 234	8.7 225	0-0.1	2.2 264	0.3	No cloud		LaRC: ice and liquid water MOD06: no cloud
17/3/03	1100	284	6.8 238	7.8 231	0.1	3.6 257	0.4	No cloud	1	LaRC: ice and liquid water MOD06: ice
27/3/03	1140	291	9.8 220	10.1 214	0.06	No cloud		No cloud		LaRC and MODIS: no cloud
1/4/03*	1020	288	9.4 224	10.7 214	0.15-0.8	7.4 239	1.3	No ice	1.7	LaRC: ice and liquid water MOD06: ice and liquid water
9/9/03*	1100	292	9.2 230	10.1 224	0.09-0.1	6.6 248	1.3	16.4 ?	1.8	LaRC: ice and liquid water MOD06: ice and liquid water
15/9/03	1200	295	11.7 220	12 218	0.03	No cloud		No cloud		LaRC and MODIS: no cloud
6/11/03	1140	287	10.3 225	11.2 217	0-0.1	No cloud		11.3 218	No cloud	LaRC and MODIS: no cloud
17/11/03*	1120	282	9.3 227	11.2 213	0.05-0.1	5.6 249	0.6	No cloud	2.8	LaRC: ice and liquid water MOD06: ice and liquid water
9/12/03	1040	278	9.3 227	11.2 213	0.1-0.2	2.5 261	0.3	No cloud		LaRC: ice and liquid water MOD06: no cloud

* When the comparison of the 3 methods is possible (semi-transparent cloud for CALIPSO-like technique and ice cloud found for LaRC and MOD06 techniques)

Table 4: Results of the three retrieval methods for 8 October 2002 case.

method	altitude (km)	temperature (K)	optical thickness	particle effective radius (μm)
CALIPSO-like	6.1 - 11	251 - 214	1.4 - 3.0	6 - 22
LaRC	6.9 - 8.7	245 - 231	1.8 ± 0.5	19 ± 4.5
MOD06	9.7 (top)	222 (top)	2.2 ± 0.5	14 - 37

Table 5: Tropical ice clouds cases during CRYSTAL-FACE.

Day (July 2002) Start-stop times (UTC)	Sfc temp (K) ¹ Leg #	CALIPSO-like (MAS)			LaRC (GOES)			MAS (MAS)		Comments
		Z _t Z _{max} Z _b (km)	T _t T _{max} T _b (K)	τIR ⁽³⁾ +shape class	T _c (K) GOES time (UTC)	Z _t Z _b (km)	τ	Z _t (km)	τ	
23 18.641 18.655	302 #1	13.8 11.9 11.7	209 222 223	? I	224 18.42	11.7 11-12 6.8	27.9 14-35	12.2	0-35	Thick cloud. LaRC: ice MAS: ice
23 18.858 18.870	302 #2	13.6 11.7 11.5	209 224 225	? I	225 18.42	11.6 11.3-12 7.0	18.9 11-22	12.2	6-8	Thick cloud. LaRC: ice MAS: ice
23 19.085 19.091	301 #3	10.1 8.79 8.5	237 247 250	? I	250 18.92	8.3 8.3 4.9	16.9 16.9	10.9	5-10	Thick cloud. LaRC: ice MAS: ice
26 18.300 18.359	303 #4	15.4 12.5	200 218	0.25-1 II	259 17.9	7.5 5-10 7	0.87 0.7-1	10.9	0-9	Thin ice cloud, possible low layer LaRC: water + ice MAS: multi ice
26 18.482 18.500	303 #5	15.4 12.5	200 218	0.1-0.5 I, II, III	232 18.75	11.7 9-15.7 10.4	0.87 0.5-1.4	10.9	0-17	Thin ice cloud, possible low layer LaRC: ice MAS: multi-layer ice+water+clear
26 19.000 19.079	303 #6	15.4 12.4	200 218	0.5-2 I, II, III	254 18.75	8.7 6-13 7.7	1.3 0.5-2	10.9	0-8	Thin ice cloud LaRC: ice MAS: single-layer ice + multi mixed
28 21.575 21.578	303 #7	14.6 13.4 13.3	206 212 213	? II	216 21.59	12.8 12.8 6.7	68 57-71	14.5	5-48	Thick cloud. LaRC: ice MAS: ice
28 22.296 22.321	303 #8	14.6 11.6 11.2	209 226 225	0.25-3 I, II	260 22.32	9.8 8.5 5-12.7	1.3 0.5-1.9	10.8	1-3	Possible low layer LaRC: water/ice/ MAS: ice
28 22.945 22.973	303 #9	14.4 13 13	210 215 215	No data	220 22.99	12.4 11-13 7.7	21.5 7-44	13.5	1-46	Missing MAS data LaRC: ice MAS: ice
29 15.702 15.710	304 #10	11.9 10.3 10.3 +5.7-6	222 233 233 +263	0.5-10 I	260 15.67	7.7 7.2-7.8 6.6	2.9 2-5	10.7	4-45	CALIPSO-like: + low layer LaRC: ice MAS: single ice + multi- layer mixed
29 15.811 15.823	304 #11	11.9 10.5 +5-5.5	222 231 +267	>2 I	261 15.75	7.6 7.6 6.3	3.9 3.9	10.7	2-6	CALIPSO-like: + low layer Ambiguous phase LaRC: water MAS: water
29 19.814 19.827	304 #12	13.5 13.1 12.5	215 218 221	? I	219 19.75	12.5 12.5 6	128 128	14.5	20-62	Thick anvil LaRC: ice MAS: ice
29 20.300 20.322	304 #13	13.5 12.5 12.5	215 221 221	2-10 I, II, III	250 20.25	9.5 6-12 7.8	2.5 1-3	10.7	3-5	Thick anvil. No CALIPSO- like model match LaRC: ice MAS: ice
29 20.424 20.440	304 #14	13.5 12.5 12.5	215 221 221	1-10 I, II, III	248 20.25	9.9 7-11 8.1	2.3 1-4	10.7	2-5	Thick anvil. No CALIPSO- like model match LaRC: ice MAS: ice

¹temperature of dropsonde lowest layer

²altitude and temperature of maximum lidar backscattered signal (altitude taken into account in the radiative transfer calculation for the CALIPSO-like method)

³for CALIPSO-like method, optical thickness is from the radiative transfer calculation compared to the observation because clouds are often too thick to retrieve the optical thickness directly from the lidar.

Table 6: Results of the three retrieval methods for flight leg 8, mean with range in parentheses.

method	altitude (km)	temperature (K)	optical thickness	particle effective radius (μm)
CALIPSO-like	(11.2 - 14.6)	(209.0 - 225.0)	(0.25 – 3.0)	(22- 32)
LaRC	9.8 (5.3-12.7)	248.0 (234 -268)	1.3 (0.5 – 1.9)	27.8 (22-40)
MAS	10.8	—	1 - 3	(31 - 38)

Table 7: Comparison between $r_{e,In-Situ}$ averaged over 10 minutes, $r_{e,CAL-like}$, $r_{e,LaRC}$, and $r_{e,MAS}$ for the 5 flight legs with coincidence between the ER-2 and WB-57 flight paths.

Flight leg	coincidence time (min)	$r_{e,In-Situ}$ (μm)	$r_{e,CAL-like}$ (μm)	$r_{e,LaRC}$ (μm)	$r_{e,MAS}$ (μm)
7	+ 20	25.2 (std 14.2) uncertainty: ± 10.1	—	32.8-34.1	22.3 - 25.9
8	- 22	34.4 (std 32.4) uncertainty: ± 13.7	22 - 32	19.6 - 40	31.1 - 38.3
12	+ 14	43.1 (std 21.1) uncertainty: ± 17.2	—	31.3 - 33.8	23.4 - 25.7
13	- 14	35.3 (std 24.2) uncertainty: ± 14.1	—	14.6 – 22.6	32 - 39.9
14	- 22	37.5 (std 24.1) uncertainty: ± 15	—	16.4 - 19.8	32.6 - 39.7

Figure captions

Figure 1: October 8th 2002: (a) lidar depolarization ratio, (b) composite image using 0.6-, 1.6-, 11- μm channels from LaRC retrieval using MODIS data at 1105 UT, (c) LaRC cloud phase: '1' is water cloud, '2' is ice cloud, '3' is no retrieval, '4' is clear, '5' is bad data, '6' is no retrieval water cloud, '7' is no retrieval ice cloud. SIRTa area is the center of red square.

Figure 2: τ_{MOD06} retrieved in the 5x5 pixels area against τ_{MOD06} retrieved in the 3 pixels-large wind strip, for SIRTa cases. Errorbars are standard deviations calculated in the sample of pixels.

Figure 3: SIRTa cloud cases (a) $T_{\text{CAL-like}} = f(T_{\text{LaRC}})$, (b) $T_{\text{CAL-like}} = f(T_{\text{MOD06}})$, (c) $T_{\text{MOD06}} = f(T_{\text{LaRC}})$, (d) probability density function of $T_{\text{CAL-like}} - T_{\text{LaRC}}$, (e) PDF of $T_{\text{CAL-like}} - T_{\text{MOD06}}$, (f) PDF of $T_{\text{MOD06}} - T_{\text{LaRC}}$. Dashed lines are $x = y$.

Figure 4: SIRTa cloud cases (a) $z_{\text{CAL-like}} = f(z_{\text{LaRC}})$, (b) $z_{\text{CAL-like}} = f(z_{\text{MOD06}})$, (c) $z_{\text{MOD06}} = f(z_{\text{LaRC}})$, (d) probability density function of $z_{\text{CAL-like}} - z_{\text{LaRC}}$, (e) PDF of $z_{\text{CAL-like}} - z_{\text{MOD06}}$, (f) PDF of $z_{\text{MOD06}} - z_{\text{LaRC}}$. Dashed lines are $x = y$.

Figure 5: SIRTa cloud cases: (a) $T_{\text{CAL-like}} - T_{\text{LaRC}} = f(\tau_{\text{CAL-like}})$, (b) $z_{\text{CAL-like}} - z_{\text{LaRC}} = f(\tau_{\text{CAL-like}})$.

Figure 6: SIRTa cloud cases (a) $\tau_{\text{CAL-like}} = f(\tau_{\text{LaRC}})$, (b) $\tau_{\text{CAL-like}} = f(\tau_{\text{MOD06}})$, (c) $\tau_{\text{LaRC}} = f(\tau_{\text{MOD06}})$, (d) probability density function of $\tau_{\text{CAL-like}} - \tau_{\text{LaRC}}$, (e) probability density function of $\tau_{\text{CAL-like}} - \tau_{\text{MOD06}}$, (f) probability density function of $\tau_{\text{LaRC}} - \tau_{\text{MOD06}}$. Dashed lines are $x = y$. Errorbars are standard deviations.

Figure 7: SIRTa cloud cases: (a) $r_{e,\text{CAL-like}} = f(r_{e,\text{LaRC}})$, (b) $r_{e,\text{CAL-like}} = f(r_{e,\text{MOD06}})$, (c) $r_{e,\text{LaRC}} = f(r_{e,\text{MOD06}})$, (d) probability density function of $r_{e,\text{CAL-like}} - r_{e,\text{LaRC}}$, (e) probability density function of $r_{e,\text{CAL-like}} - r_{e,\text{MOD06}}$, (f) probability density function of $r_{e,\text{LaRC}} - r_{e,\text{MOD06}}$. Dashed lines are $x = y$. Errorbars are standard deviation.

Figure 8: July 28th flight leg from 22:17:47 to 22:19:17. (a) CPL depolarization ratio, (b) GOES visible image, (c) optical thickness retrieved from MAS data using MAS method, (d) optical thickness derived from GOES-8 using LaRC method. Red arrow is the considered flight leg.

Figure 9: CRYSTAL-FACE cases for the ones CALIPSO-like retrieval is not possible: $r_{e,MAS} = f(r_{e,LaRC})$. Dashed line is $x = y$. Errorbars are standard deviations.

Figure 10: CRYSTAL-FACE cloud cases (a) $T_{CAL-like} = f(T_{LaRC})$, (b) probability density function of $T_{CAL-like} - T_{LaRC}$, (c) $z_{CAL-like} = f(z_{LaRC})$ in X, $z_{CAL-like} = f(z_{MAS})$ in O, $z_{LaRC} = f(z_{MAS})$ in V, (d) probability density function of $z_{CAL-like} - z_{LaRC}$, probability density function of $z_{CAL-like} - z_{MAS}$, probability density function of $z_{LaRC} - z_{MAS}$. Dashed lines are $x = y$.

Figure 11: CRYSTAL-FACE cloud cases (a) $\tau_{IR,CAL-like} = f(\tau_{LaRC})$, (b) $\tau_{IR,CAL-like} = f(\tau_{MAS})$, (c) $\tau_{LaRC} = f(\tau_{MAS})$, (d) probability density function of $\tau_{IR,CAL-like} - \tau_{LaRC}$, (e) probability density function of $\tau_{IR,CAL-like} - \tau_{MAS}$, (f) probability density function of $\tau_{LaRC} - \tau_{MAS}$. Dashed lines are $x = y$ and dotted lines are $x=2y$. Errorbars are standard deviation.

Figure 12: CRYSTAL-FACE cloud cases: (a) $r_{e,CAL-like} = f(r_{e,LaRC})$, (b) $r_{e,CAL-like} = f(r_{e,MAS})$, (c) $r_{e,LaRC} = f(r_{e,MAS})$, (d) probability density function of $r_{e,CAL-like} - r_{e,LaRC}$, (e) probability density function of $r_{e,CAL-like} - r_{e,MAS}$, (f) probability density function of $r_{e,LaRC} - r_{e,MAS}$. Dashed lines are $x = y$. Errorbars are standard deviation.

Figure 13: Thermodynamical phase detected by LaRC (in white) and MOD06/MAS methods when CALIPSO-like method leads to ice.

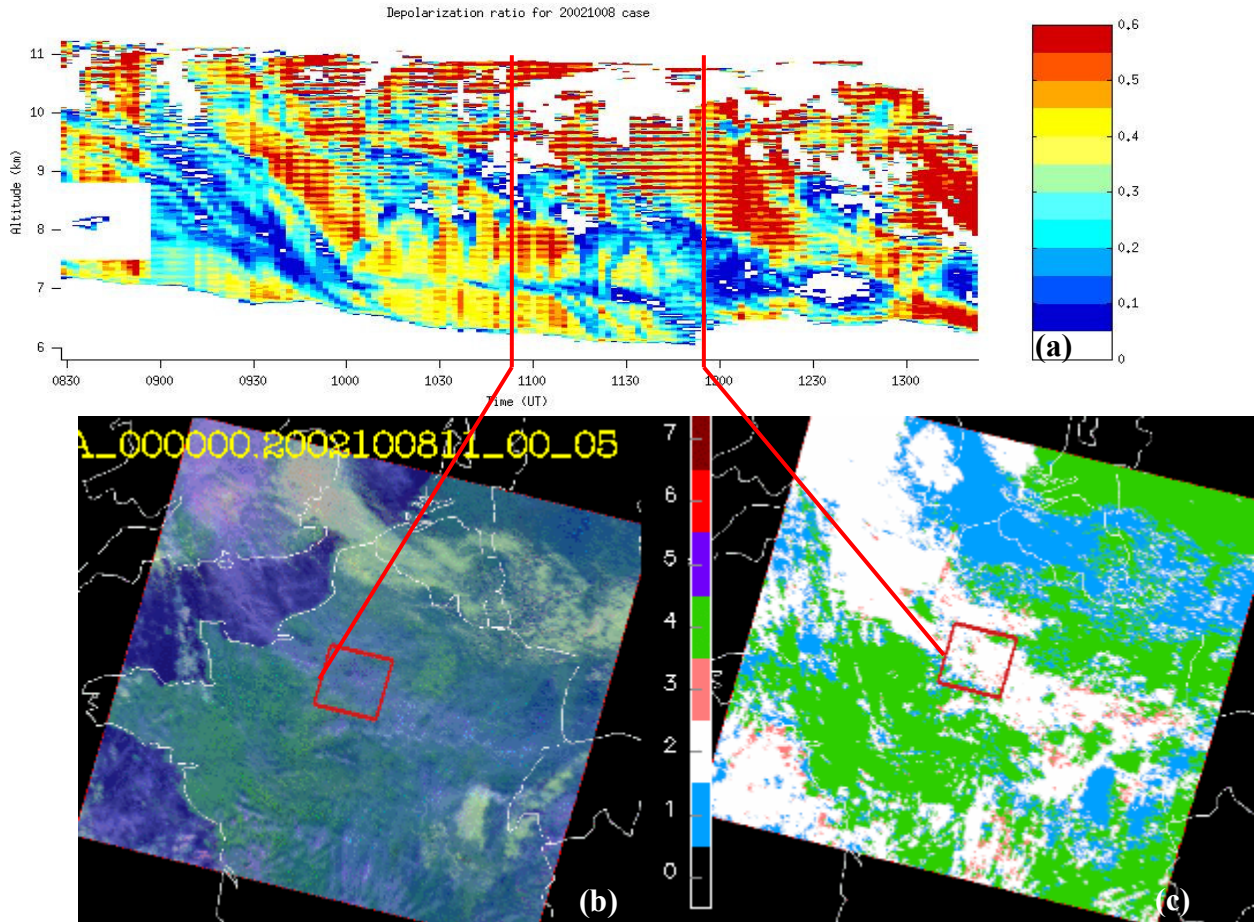


Figure 1: October 8th 2002: (a) lidar depolarization ratio, (b) composite image using 0.6-, 1.6-, 11- μ m channels from LaRC retrieval using MODIS data at 1105 UT, (c) LaRC cloud phase: '1' is water cloud, '2' is ice cloud, '3' is no retrieval, '4' is clear, '5' is bad data, '6' is no retrieval water cloud, '7' is no retrieval ice cloud. SIRTA area is the center of red square.

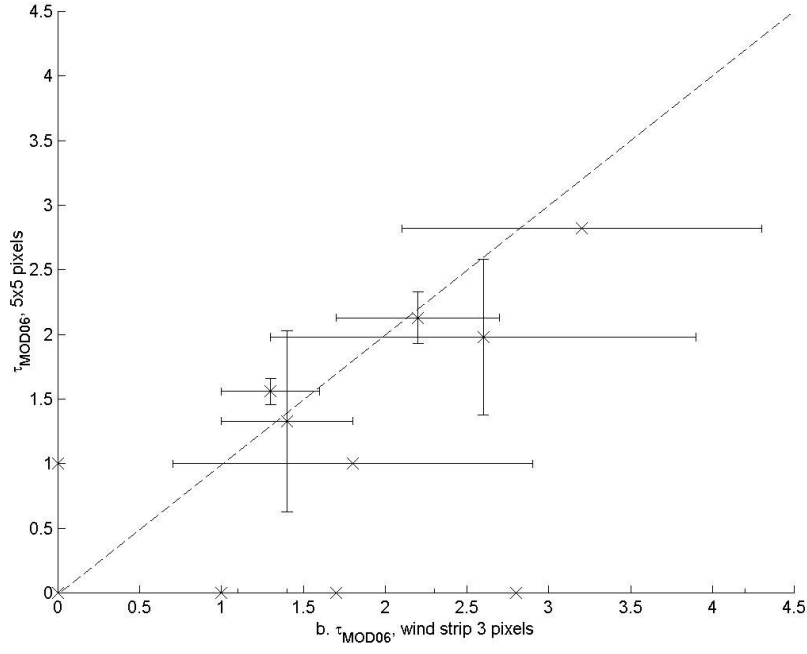


Figure 2: τ_{MOD06} retrieved in the 5x5 pixels area against τ_{MOD06} retrieved in the 3 pixels-large wind strip, for SIRTa cases. Errorbars are standard deviations calculated in the sample of pixels.

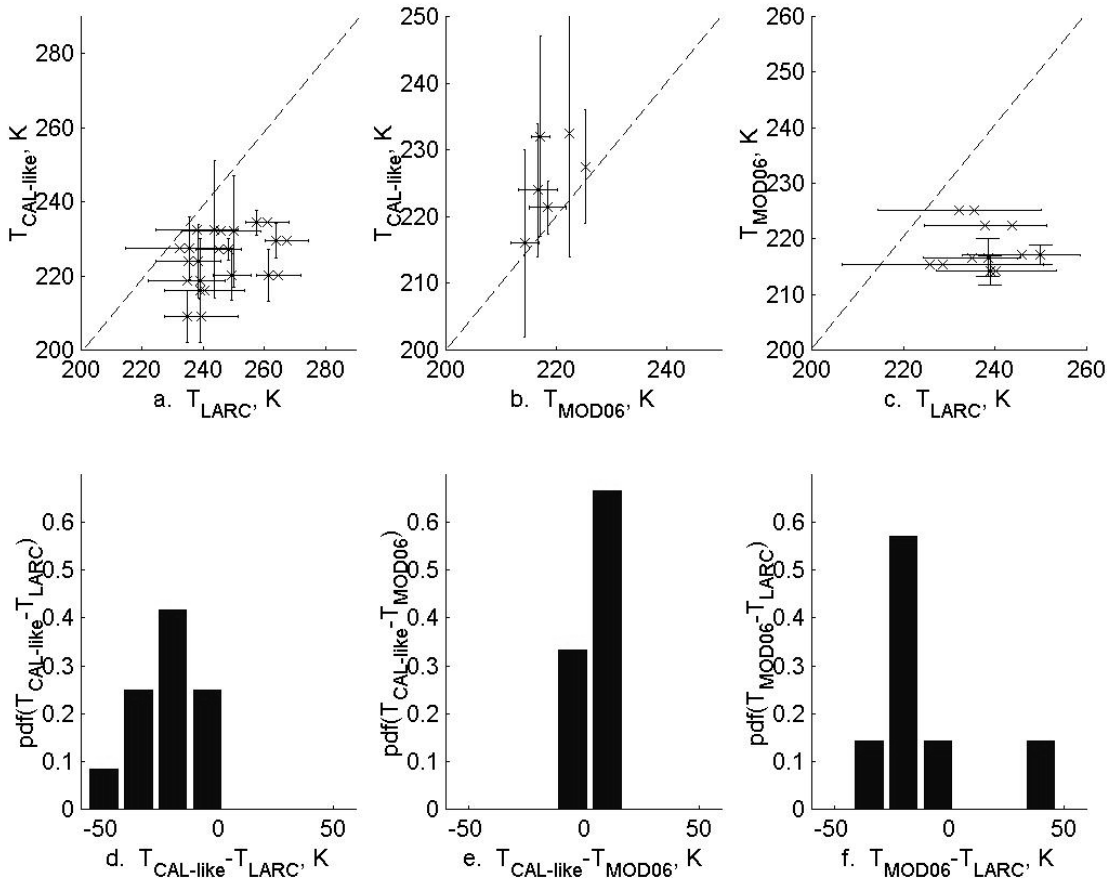


Figure 3: SIRT cloud cases (a) $T_{\text{CAL-like}} = f(T_{\text{LaRC}})$, (b) $T_{\text{CAL-like}} = f(T_{\text{MOD06}})$, (c) $T_{\text{MOD06}} = f(T_{\text{LaRC}})$, (d) probability density function of $T_{\text{CAL-like}} - T_{\text{LaRC}}$, (e) PDF of $T_{\text{CAL-like}} - T_{\text{MOD06}}$, (f) PDF of $T_{\text{MOD06}} - T_{\text{LaRC}}$. Dashed lines are $x = y$.

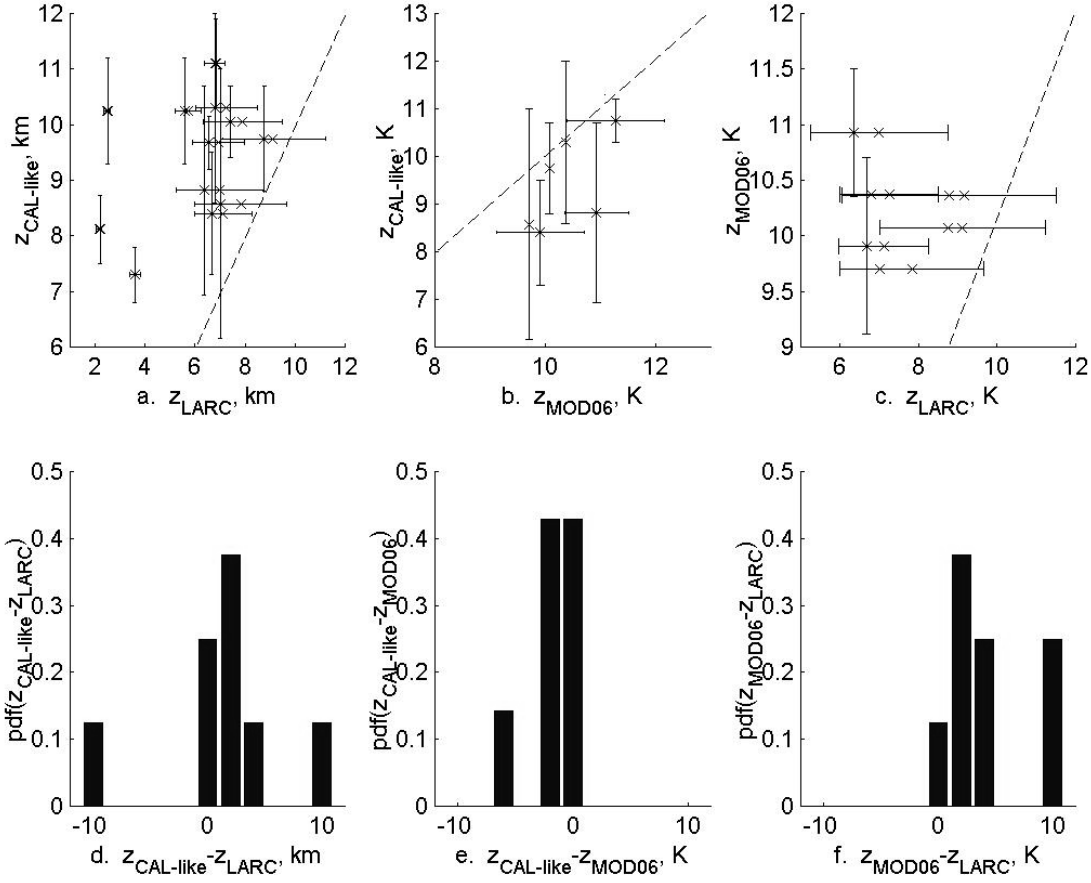


Figure 4: SIRT cloud cases (a) $z_{\text{CAL-like}} = f(z_{\text{LARC}})$, (b) $z_{\text{CAL-like}} = f(z_{\text{MOD06}})$, (c) $z_{\text{MOD06}} = f(z_{\text{LARC}})$, (d) probability density function of $z_{\text{CAL-like}} - z_{\text{LARC}}$, (e) PDF of $z_{\text{CAL-like}} - z_{\text{MOD06}}$, (f) PDF of $z_{\text{MOD06}} - z_{\text{LARC}}$. Dashed lines are $x = y$.

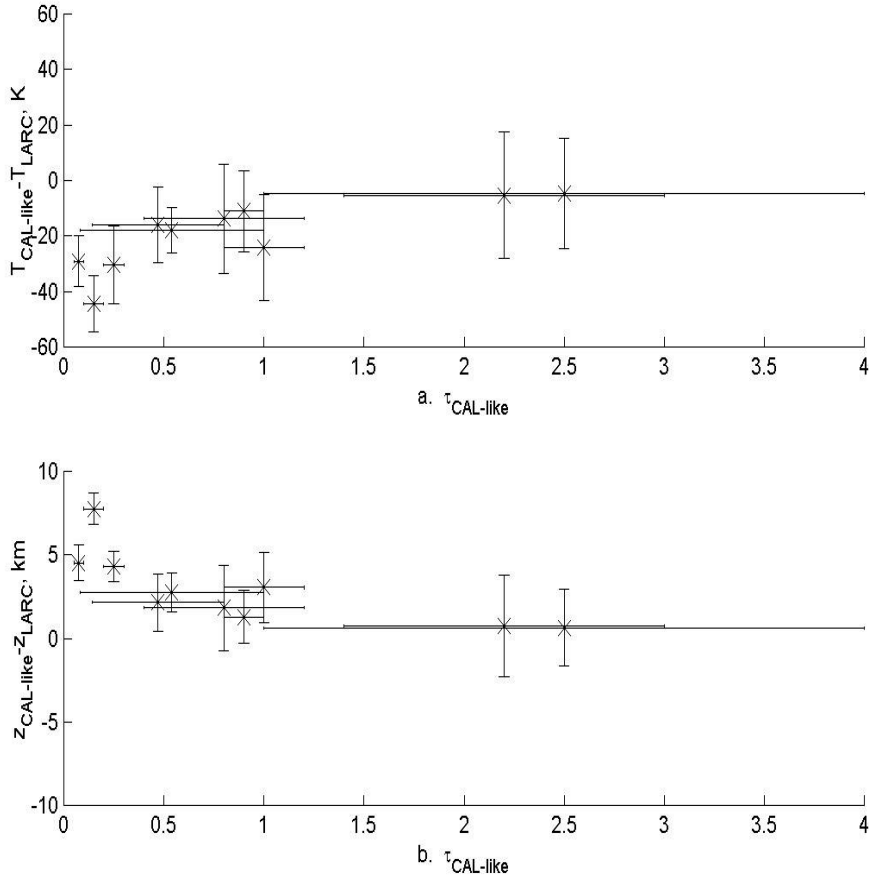


Figure 5: SIRTa cloud cases: (a) $T_{\text{CAL-like}} - T_{\text{LaRC}} = f(\tau_{\text{CAL-like}})$, (b) $z_{\text{CAL-like}} - z_{\text{LaRC}} = f(\tau_{\text{CAL-like}})$.

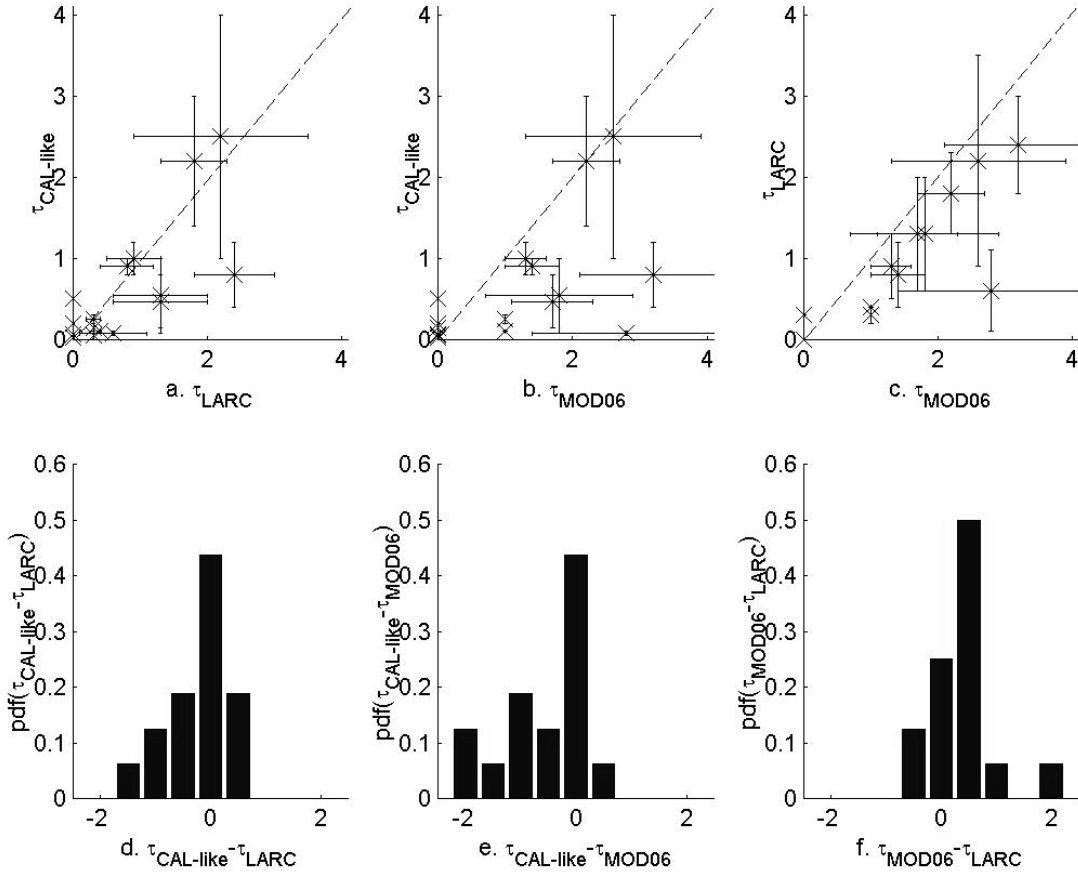


Figure 6: SIRT cloud cases (a) $\tau_{\text{CAL-like}} = f(\tau_{\text{LARC}})$, (b) $\tau_{\text{CAL-like}} = f(\tau_{\text{MOD06}})$, (c) $\tau_{\text{LARC}} = f(\tau_{\text{MOD06}})$, (d) probability density function of $\tau_{\text{CAL-like}} - \tau_{\text{LARC}}$, (e) probability density function of $\tau_{\text{CAL-like}} - \tau_{\text{MOD06}}$, (f) probability density function of $\tau_{\text{LARC}} - \tau_{\text{MOD06}}$. Dashed lines are $x = y$. Errorbars are standard deviations.

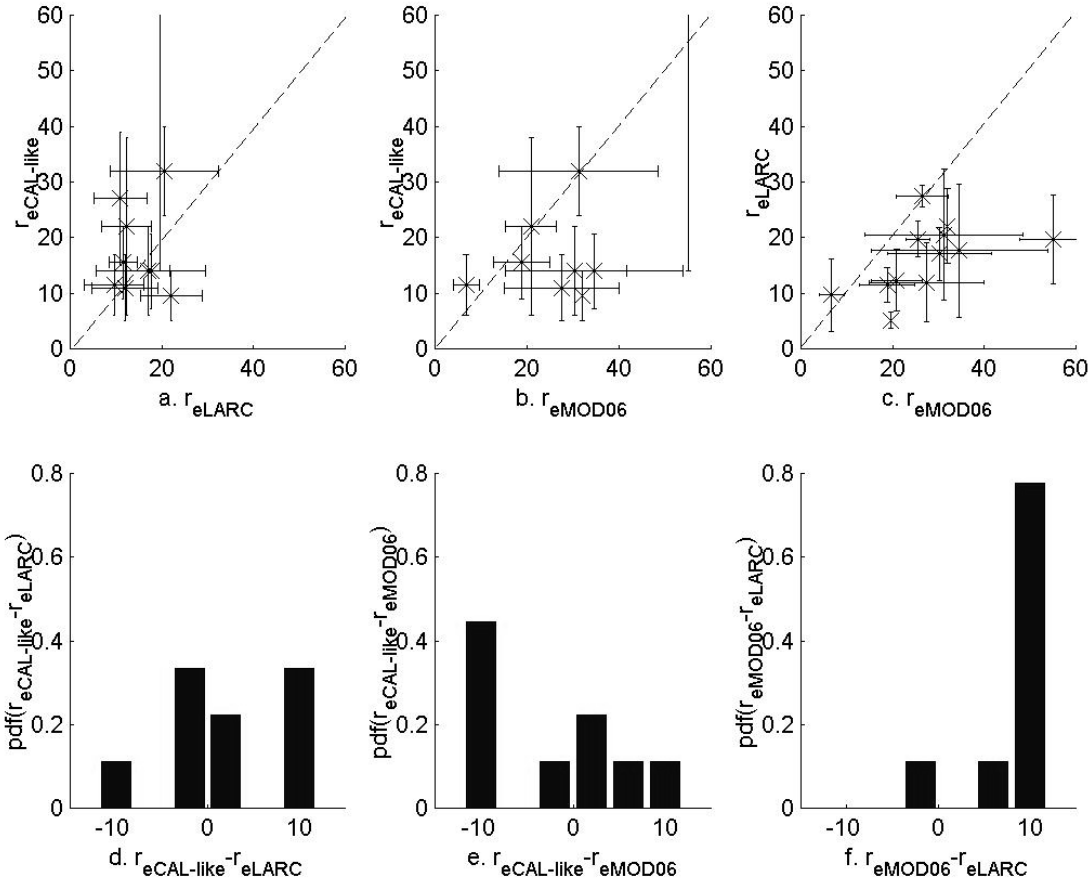


Figure 7: SIRTa cloud cases: (a) $r_{e,CAL-like} = f(r_{e,LaRC})$, (b) $r_{e,CAL-like} = f(r_{e,MOD06})$, (c) $r_{e,LaRC} = f(r_{e,MOD06})$, (d) probability density function of $r_{e,CAL-like} - r_{e,LaRC}$, (e) probability density function of $r_{e,CAL-like} - r_{e,MOD06}$, (f) probability density function of $r_{e,LaRC} - r_{e,MOD06}$. Dashed lines are $x = y$. Errorbars are standard deviation.

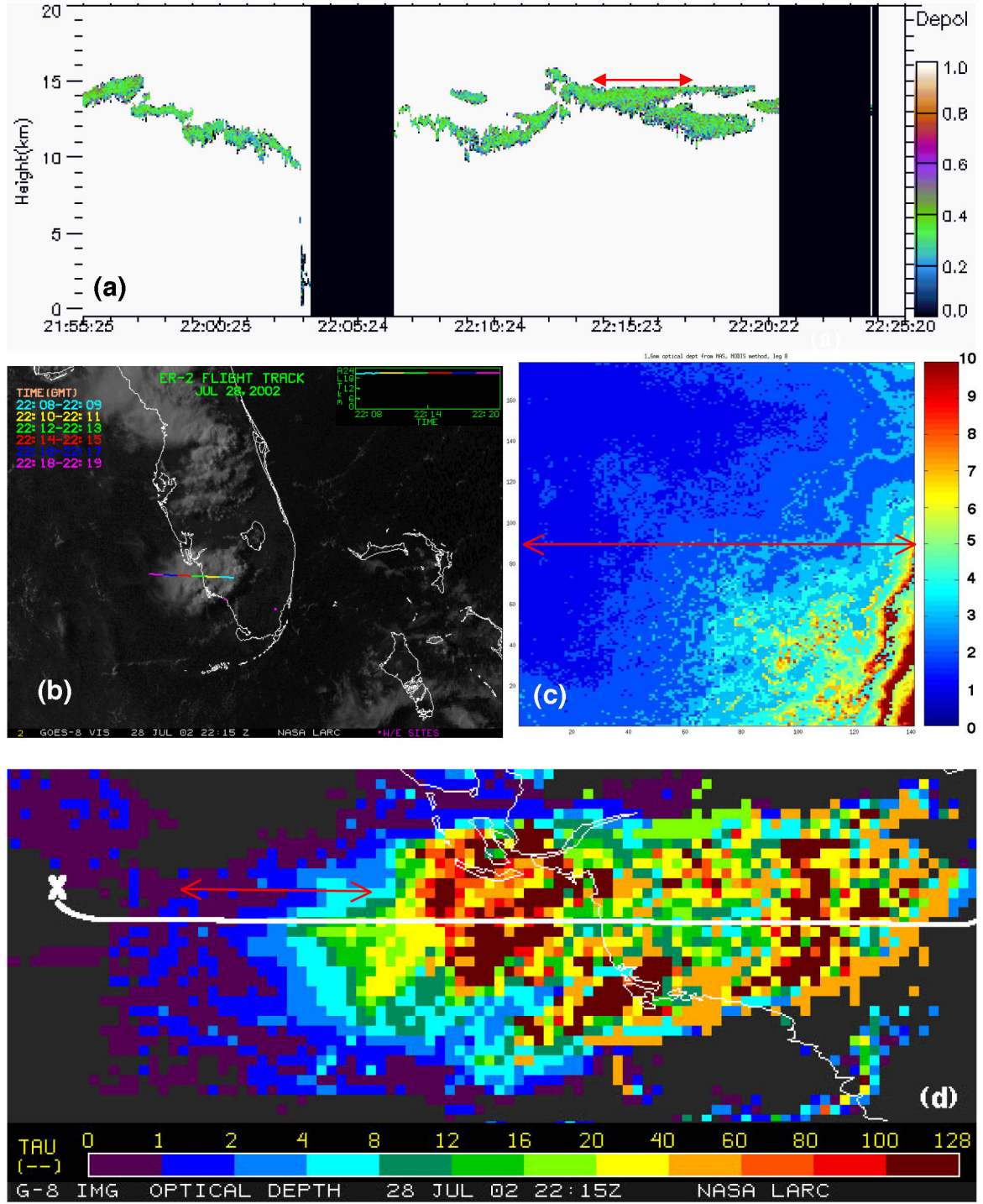


Figure 8: July 28th flight leg from 22:17:47 to 22:19:17. (a) CPL depolarization ratio, (b) GOES visible image, (c) optical thickness retrieved from MAS data using MAS method, (d) optical thickness derived from GOES-8 using LaRC method. Red arrow is the considered flight leg.

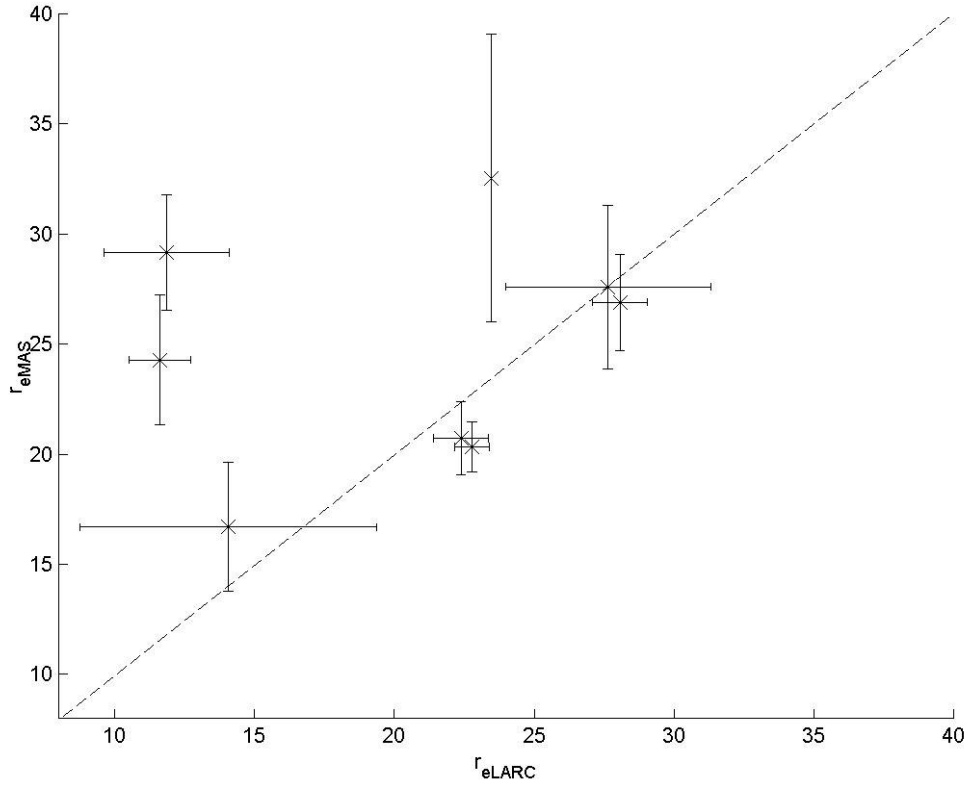


Figure 9: CRYSTAL-FACE cases for the ones CALIPSO-like retrieval is not possible: $r_{e,MAS} = f(r_{e,LARC})$. Dashed line is $x = y$. Errorbars are standard deviations.

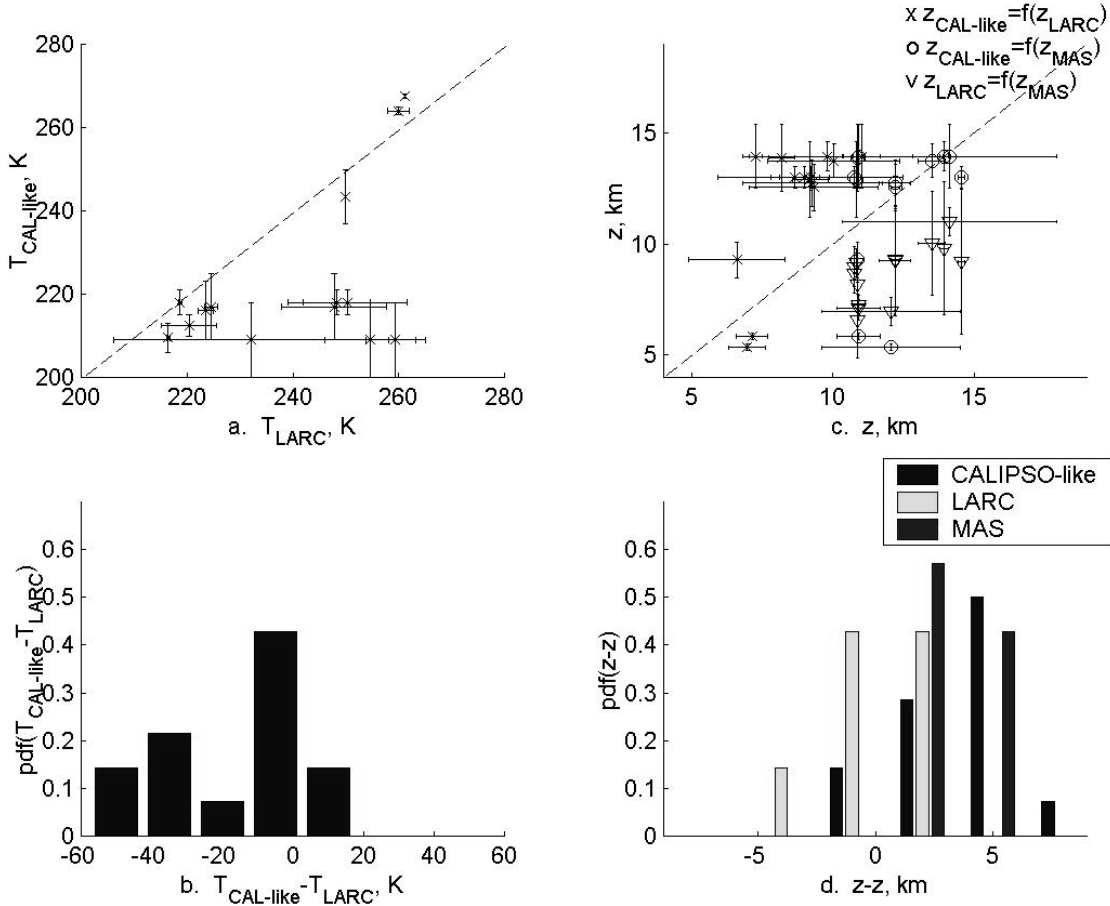


Figure 10: CRYSTAL-FACE cloud cases (a) $T_{\text{CAL-like}} = f(T_{\text{LARC}})$, (b) probability density function of $T_{\text{CAL-like}} - T_{\text{LARC}}$, (c) $z_{\text{CAL-like}} = f(z_{\text{LARC}})$ in X, $z_{\text{CAL-like}} = f(z_{\text{MAS}})$ in O, $z_{\text{LARC}} = f(z_{\text{MAS}})$ in V, (d) probability density function of $z_{\text{CAL-like}} - z_{\text{LARC}}$, probability density function of $z_{\text{CAL-like}} - z_{\text{MAS}}$, probability density function of $z_{\text{LARC}} - z_{\text{MAS}}$. Dashed lines are $x = y$.

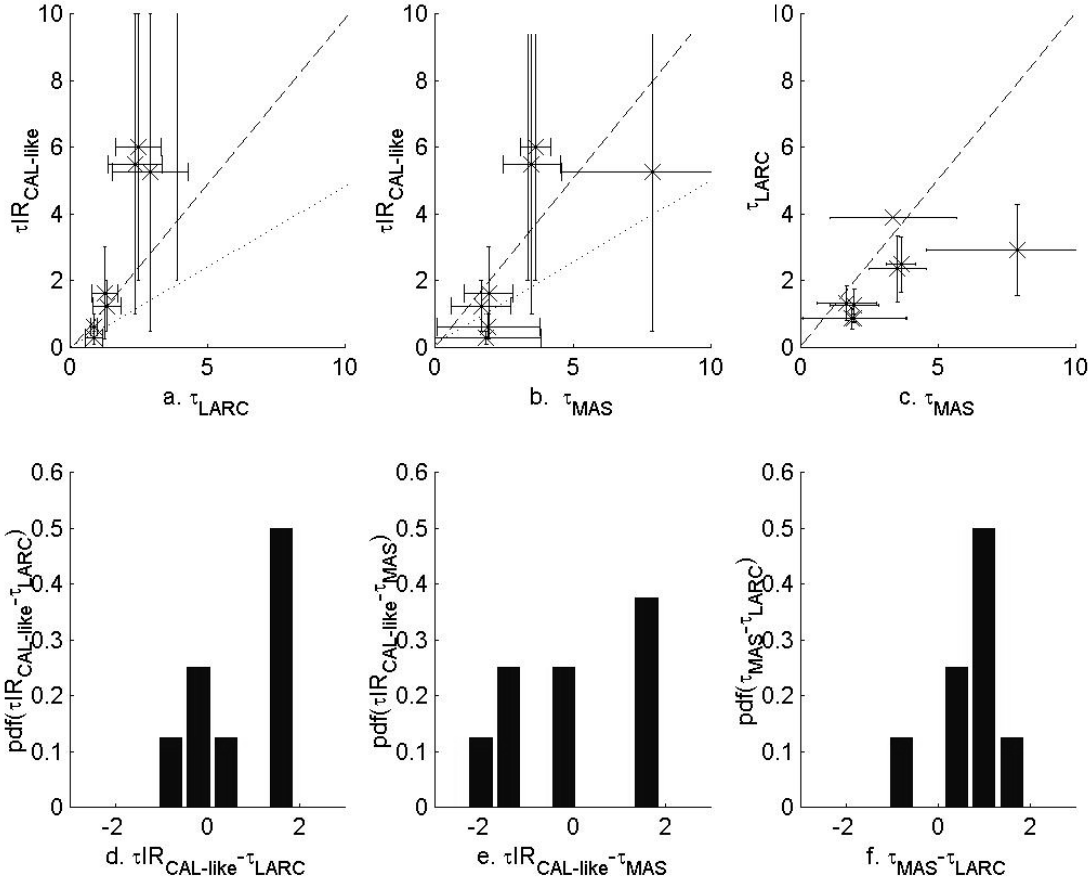


Figure 11: CRYSTAL-FACE cloud cases (a) $\tau_{IR_CAL-like} = f(\tau_{LARC})$, (b) $\tau_{IR_CAL-like} = f(\tau_{MAS})$, (c) $\tau_{LARC} = f(\tau_{MAS})$, (d) probability density function of $\tau_{IR_CAL-like} - \tau_{LARC}$, (e) probability density function of $\tau_{IR_CAL-like} - \tau_{MAS}$, (f) probability density function of $\tau_{LARC} - \tau_{MAS}$. Dashed lines are $x = y$ and dotted lines are $x = 2y$. Errorbars are standard deviation.

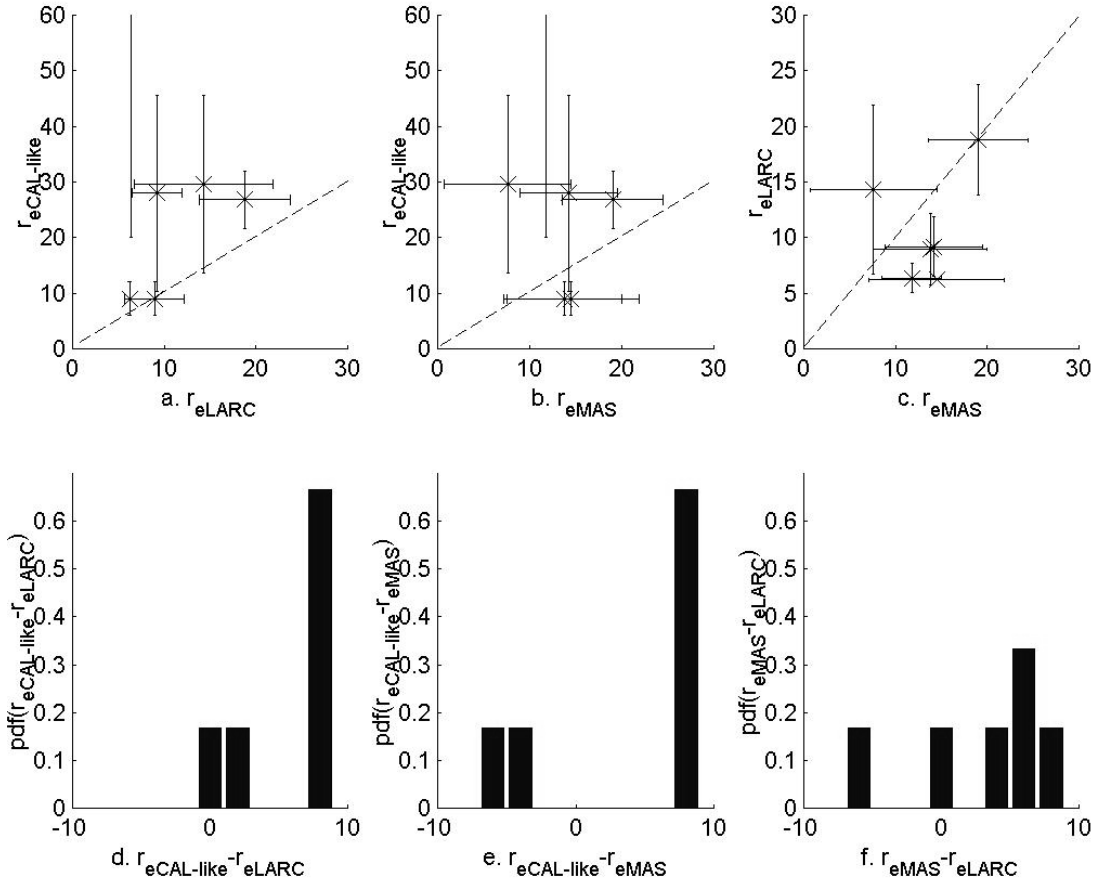


Figure 12: CRYSTAL-FACE cloud cases: (a) $r_{e,CAL-like} = f(r_{e,LaRC})$, (b) $r_{e,CAL-like} = f(r_{e,MAS})$, (c) $r_{e,LaRC} = f(r_{e,MAS})$, (d) probability density function of $r_{e,CAL-like} - r_{e,LaRC}$, (e) probability density function of $r_{e,CAL-like} - r_{e,MAS}$, (f) probability density function of $r_{e,LaRC} - r_{e,MAS}$. Dashed lines are $x = y$. Errorbars are standard deviation.

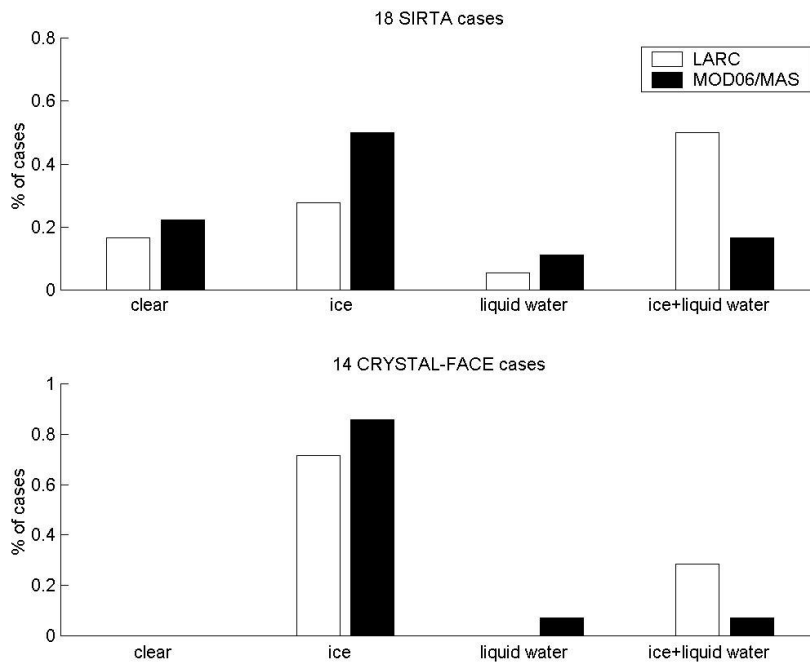


Figure 13: Thermodynamical phase detected by LaRC (in white) and MOD06/MAS methods when CALIPSO-like method leads to ice.